EXPLORING THE SUSCEPTIBILITY TO CARDIAC ARRHYTHMIAS AND UNDERLYING MECHANISMS IN PULMONARY ARTERIAL HYPERTENSION

by

Tony Eli El-Rabahi

Submitted in partial fulfilment of the requirements for the degree of Master of Science

at

Dalhousie University
Halifax, Nova Scotia
June 2023

Dalhousie University is located in Mi'kma'ki, the ancestral and unceded territory of the Mi'kmaq. We are all Treaty people.

TABLE OF CONTENTS

LIST OF TABLES

LIST OF FIGURES

ABSTRACT

Background: Pulmonary arterial hypertension (PAH) is a progressive incurable disease with unclear etiology. Primary cause of death in PAH patients is right (-sided) heart failure, occurring as a direct consequence of increased right ventricular (RV) afterload. Importantly, around 25% of these deaths have been linked to cardiac arrhythmias. However, mechanisms underlying arrhythmia susceptibility in patients with elevated pulmonary arterial and RV pressure remains unclear.

Methods: Male Fischer CDF rats were treated with monocrotaline (MCT; 60 mg/kg, s.c) to induce PAH or treated with vehicle as control. Echocardiography was performed at experimental endpoint (4 and 5 weeks post-MCT injection) to assess disease progression. Electrocardiogram was recorded in anesthetized rats after echocardiography to study electrical abnormality and assess spontaneous arrhythmias during progressive PAH. At 4 and 5 weeks, hearts were collected, perfused using Langendorff apparatus, and electrical remodeling was assessed by optical mapping. The hearts were paced electrically with increasing frequency and electrophysiological parameters were recorded.

Results: MCT treatment led to progressive increase in RV systolic pressure and RV hypertrophy at 4- and 5-week time-points, compared to controls. Action potential duration (APD) was increased in response to RV remodeling at 4-week with marked increase at 5-week time-point. Reduced vascular density was observed at the 5-week time-point.

Conclusions: PAH in Fischer rats treated with MCT was associated with electrical remodeling and reduced vascular density. These changes in RV may contribute to increased susceptibility to arrhythmias and sudden death in PAH.

LIST OF ABBREVIATIONS USED

AP	Action potential
APD	Action potential duration
μ	Action potential duration heterogeneity index
AV	Atrioventricular
ANS	Autonomic nervous system
BMPR2	Bone morphogenic protein receptor-2
CCB	Calcium channel blocker
CACF	Carleton Animal Care Facility
CCAC	Canadian Council of Animal Care
CI	Cardiac index
CO	Cardiac output
CTEPH	Chronic thromboembolic PH
CD31	Cluster of differentiation 31
CV	Conduction velocity
CHD	Congenital heart disease
CSA	Cross-sectional area
cGMP	Cyclic guanosine monophosphate
DAB	Diaminobenzidine
ET_A	ET-1 Receptor A
ET_B	ET-1 Receptor B
EAD	Early after depolarization
EF	Ejection fraction

ECG	Electrocardiogram/electrocardiography
EC	Endothelial cell
ET-1	Endothelin-1
FAC	Fractional area change
FS	Fractional shortening
HR	Heart rate
H&E	Hematoxylin & Eosin
HPAH	Heritable PAH
HIV	Human immunodeficiency virus
HCl	Hydrochloric acid
IPAH	Idiopathic PAH
IHC	Immunohistochemistry
LA	Left atrium
LV	Left ventricle
LVIDd	Left ventricular interior diameter during diastole
MCT	Monocrotaline
NO	Nitric oxide
NOS	Nitric oxide synthase
PCL	Pacing cycle length
PFA	Paraformaldehyde
PDE-5i	Phosphodiesterase-5 inhibitor
PECAM-1	Platelet and endothelial cell adhesion molecule-1
PGI_2	Prostacyclin

PAH	Pulmonary arterial hypertension
PAP	Pulmonary arterial pressure
PA	Pulmonary artery
PAAT	Pulmonary artery acceleration time
PA-VTI	Pulmonary artery velocity-time integral
PAWP	Pulmonary artery wedge pressure
PET	Pulmonary ejection time
PH	Pulmonary hypertension
PVR	Pulmonary vascular resistance
ROS	Reactive oxygen species
ROI	Region of interest
RA	Right atrium
RV	Right ventricle
RHF	Right heart failure
RVAW	Right ventricle anterior wall
RVAd	Right ventricular area during diastole
RVAs	Right ventricular area during systole
RVFWT	Right ventricular free-wall thickness
RVH	Right ventricular hypertrophy
RVIDd	Right ventricular interior diameter during diastole
RVSP	Right ventricular systolic pressure
S	Septum
SMC	Smooth muscle cell

NaOH	Sodium hydroxide
SD	Sprague-Dawley rat strain
St.Dev	Standard deviation
SV	Stroke volume
Sugen/SU-5416	Sugen-5416
SU/Hx	Sugen-Hypoxia
UCLA	University Committee Laboratory Animals
dF/dt_{max}	Upstroke velocity
VEGF	Vascular endothelial growth factor
VEGFR-2	Vascular endothelial growth factor receptor 2
VF	Ventricular fibrillation
WHO	World Health Organization
VF	Ventricular fibrillation
VT	Ventricular tachycardia

ACKNOWLEDGEMENTS

The effort, work, and dedication that this thesis contains would not have been possible without the support and guidance of those around me. I would like to thank my supervisor, Dr. Ketul R. Chaudhary for the opportunity to pursue a master's degree in cardiovascular physiology.

I would also like to thank Dr. Alex Quinn for his pivotal role as a mentor on this project. Your mentorship, guidance, and time spent introducing me to the field of cardiac electrophysiology is appreciated and will be remembered. I would like to extend my appreciation and gratitude to the former and current members of the Quinn Lab for their technical support but also their kindness and friendship.

To the rest of my supervisory committee, Dr. El-Hiani and Dr. Kienesberger, I would like to thank you for your constructive feedback, guidance, and support throughout my degree. I also want to extend my thanks to Dr. Susan Howlett for access to the equipment and tools needed to conduct my echocardiography and electrocardiography and to Peter Nicholl for his tutorials.

I would like to acknowledge the time and work that was done by the Carleton Animal Care Facility, who prioritize health and welfare of the animals involved in my research. Without their training, time, and effort, my project would not have been possible. I would like to thank DMRF and DalCREW for their generous funding and support.

Beyond the lab, I would like to thank Dr. Liz Cowley for her support and guidance during my degree. I want to thank you for making students feel recognized, valued, and accounted for. To Jill, Kate, and Sandra, thank you for your assistance with the administrative tasks I came so often to you about. And finally, to the former and current

students and staff of the Chaudhary lab, I thank you for your support, guidance, and friendship both inside and outside the lab.

CHAPTER 1: INTRODUCTION

1.1 Overview of the Heart and the Right Ventricle

The human heart is constructed of 4 distinct chambers: the left and right atria (LA and RA, respectively) and the left and right ventricles (LV and RV, respectively). Each chamber and side carry out specific function. The focus of this thesis is on the RV. The RV is the chamber located in the bottom right quadrant of the heart and is responsible for pumping blood into the pulmonary circulation.

1.1.1 RV Anatomy, Development, and Function

During fetal development, the RV is the heart's dominant chamber and is responsible for circulating blood in fetal circulation. During this stage, the RV functions under relatively higher pressures than it does in an adult heart [1], [2]. After birth, the function of the RV changes. In healthy individuals, the pulmonary circulation is a low pressure, low resistance system that is responsible for blood-gas exchange [1]. De-oxygenated blood is carried through the pulmonary arteries from the RV to the lungs for re-oxygenation at the capillary level. Carbon dioxide in the pulmonary circulation is exchanged for oxygen from the lungs. Following gas exchange, the re-oxygenated blood is taken to the LA via the pulmonary veins. Once the blood reaches the LA, the blood flows down the pressure gradient into the LV, where subsequent ventricular contraction leads to ejection of blood, by way of the aorta and aortic branch, through the systemic circulation.

The structure of the RV also changes after birth; the RV undergoes reverse-remodelling and becomes a thin-walled smaller chamber. On the contrary, the LV develops

into the dominant cardiac chamber and undergoes hypertrophic remodelling to adapt to the higher pressures it faces due to higher resistance in systemic circulation [3]. The function and conditions of the RV and pulmonary circulation are distinct from those of the LV and, consequently, require specific study and focus to make appropriate conclusions.

1.2 Pulmonary Hypertension

Pulmonary hypertension (PH) is a pathophysiological state in which there is a sustained elevation in mean pulmonary arterial pressure (PAP) ($\geq$ 20 mmHg) at rest [4]. PH can be classified in different groups based on cause of disease. The classifications of PH have passed through many iterations throughout time, as our understanding of the disease deepens. The first categories of PH were created in the 1970s at the World Health Organization (WHO) conference on PH; the categories were: 1. primary PH, and 2: secondary PH due to identified causes or risk factors [5]. It was until 1998 that this classification system remained unchanged. During the second WHO conference on PH in 1998, the five-group classification system was introduced [6]. The classification of PH has retained its original structure since 1998 and has been continuously updated at subsequent meetings. As of the most recent World Symposium on PH, held in 2017, the five clinical classes of PH are as follows: Group 1, pulmonary arterial hypertension (PAH); Group 2, PH due to left heart disease; Group 3, PH due to lung diseases and/or hypoxia; Group 4, chronic thromboembolic PH (CTEPH); and Group 5, PH due to unclear multifactorial mechanisms and causes (Table 1) [7].

Table 1. Abbreviated clinical classification of pulmonary hypertension [7]**.**

1. Pulmonary arterial hypertension
    1.1. Idiopathic PAH
    1.2. Heritable PAH
    1.3. Drug and/or toxin-induced PAH
    1.4. PAH associated with:
        1.4.1. Connective tissue disease
        1.4.2. HIV infection
        1.4.3. Portal hypertension
        1.4.4. CHD
        1.4.5. Schistosomiasis
2. Pulmonary hypertension due to left heart disease
    2.1. PH due to heart failure with preserved LV ejection fraction (LVEF) (HFpEF)
    2.2. PH due to heart failure with reduced LVEF (HFrEF)
    2.3. Valvular heart disease
    2.4. Congenital/acquired cardiovascular conditions leading to post-capillary PH
3. Pulmonary hypertension due to lung diseases and/or hypoxia
    3.1. Obstructive lung disease
    3.2. Restrictive lung disease
    3.3. Other lung disease with mixed restrictive/obstructive pattern
    3.4. Hypoxia without lung disease
    3.5. Developmental lung disorders
4. Pulmonary hypertension due to pulmonary artery obstructions
    4.1. CTEPH
    4.2. Other pulmonary artery obstructions
5. Pulmonary hypertension with unclear and/or multifactorial mechanisms
    5.1. Hematological disorders
    5.2. Systemic and metabolic disorders
    5.3. Others
    5.4. Complex congenital heart disease

1.2.1 Pulmonary Arterial Hypertension

Group 1 PH, or PAH, is defined as the presence of resting mean PAP ≥ 20 mmHg, pulmonary artery wedge pressure (PAWP) ≤ 15 mmHg, and pulmonary vascular resistance (PVR) ≥ 3 woods units [7]. It is also defined as PH in the absence of any left heart disease, lung disease, or other causes of PH [8]. In previous years, the diagnosis of PAH was reliant upon an arbitrarily set mean PAP ≥ 25 mmHg [7]. This value was set due to raising concerns of overdiagnosis and over-treatment if the mean PAP threshold was any lower. However, it was later discovered that the primary cause of PAH overdiagnosis was the failure to conduct right heart catheterization to accurately assess cardiac output (CO) and PAWP [7]. Unique to only Group 1 PH, PAH mainly affects pulmonary arteries [9].

PAH is further subdivided into four sub-categories based on the underlying mechanisms and associated pathologies or diseases: 1.1, idiopathic PAH (IPAH); 1.2, heritable PAH (HPAH); 1.3, drug and/or toxin-induced PAH; and 1.4, PAH associated with connective tissue disease, human immunodeficiency virus (HIV) infection, portal hypertension, congenital heart disease (CHD), or schistosomiasis (Table 1) [7].

According to the Giessen Pulmonary Hypertension Registry, the five-year transplant-free survival rates for PAH patients is 59% (1993-2011), with 43% of the total PAH patient population having been diagnosed with IPAH [10]. The prognosis for patients with PAH remains poor despite development in disease management and therapeutic options.

1.2.1.1 PAH Pathophysiology

1.2.1.1.1 Pulmonary vascular remodeling and increase in PAP

Unique to the pulmonary circulation, it is tasked with accommodating the entire body's CO [1]-[3]. Healthy lungs can accommodate the entire CO without arterial pressure rising much greater than venous. This phenomenon occurs both at rest and during periods of increased CO, such as during bouts of exercise. The lungs' ability to handle dramatic increases in CO reflects the organization of the pulmonary vasculature; pulmonary arterioles are arranged in parallel, thus increasing the total cross-sectional area of the arterial vessels. PAH patients, however, lose this ability to accommodate increases in CO due to the pathological reduction of the cross-sectional area of the arterial bed [11]. The loss of the pulmonary microvasculature is a cause of PAH progression.

Currently, the exact mechanisms of loss of pulmonary microvasculature remain unclear; however, PAH has been linked to genetic mutations. Mutations in bone morphogenic protein receptor-2 (BMPR2), a member of transforming growth factor- β family, are the most common mutations associated with PAH. Mutations in BMPR2 account for 70-80% HPAH patients and 20% of IPAH patients. Other mutations associated with PAH include mutations in activin receptor-like kinase 1, SMAD1, SMAD4, SMAD9 and caveolin-1 [12]. Exact mechanism by which these genetic mutations or other factors lead to PAH remain unclear; however, two main hypotheses have been proposed to explain the loss of microvasculature in PAH: the cancer hypothesis and the degenerative hypothesis. According to the cancer hypothesis, various genetic and environmental factors lead to phenotype change in the pulmonary vascular smooth muscle cells (SMC) and endothelial cells (EC) to hyperproliferative and apoptosis resistant type cells. This leads to

muscularization of precapillary arterioles and formation of occlusive vascular lesions ultimately leading to loss of pulmonary microvasculature [11], [13]. On the contrary, the degenerative hypothesis suggests that the genetic and environmental factors lead to EC apoptosis causing direct loss of fragile precapillary arterioles, that are formed by single layer of EC, causing pulmonary microvascular loss [13]. As a consequence of the pulmonary vascular rarefaction, increased PVR and PAP, the RV undergoes remodeling [14].

1.2.1.1.2 RV remodeling and disease progression

In situations of chronic pressure overload, the resultant RV remodeling can have two potential outcomes, leading to either adaptive or maladaptive remodeling [15]. Adaptive remodeling is characterized by preserved RV function (maintained CO and ejection fraction (EF)) and structure (maintained RV chamber size and minimal fibrosis) [15]. On the other hand, maladaptive remodeling is characterized by impaired cardiac function (decreased CO and EF) and negative structure remodeling (RV chamber dilation and fibrosis) [15]. Maladaptive remodeling will lead to decompensated RV state which will lead to severe pathologies, heart failure, and ultimately, death.

Fibrosis and microvascular rarefaction are two important mechanisms that are involved in RV adaptation and remodeling. Myocardial fibrosis is the product of collagen depositing between cardiomyocytes [16]. The change in RV composition affects its function. Increased collagen deposits lead to increased stiffness and limited contractability, ultimately driving maladaptive, or decompensated, RV remodeling [16], [17].

Furthermore, high vascular density and angiogenesis are critical to ensure that the cardiomyocytes are receiving sufficient nutrients and supplementation. Although angiogenesis is not a primary feature of this thesis, the lack thereof can lead to accelerated disease progression. In fact, pre-clinical and clinical studies have shown that adaptive, or compensated, RV remodeling is accompanied by angiogenesis [18]. Prior data indicate that angiogenic mechanisms are upheld during adaptive RV remodeling [18]. During cases of adaptive RV remodeling, there is an increase in angiogenesis that supports the proportion of capillaries to cardiomyocyte area [15]. Despite cardiomyocyte hypertrophy, there is adequate capillary density to nourish and support the hypertrophied cardiomyocytes (Figure 1). On the other hand, maladaptive, de-compensated, RV remodeling is associated with a lack of adequate angiogenesis [18]. There is an inadequate angiogenic response that is linked to potential down-regulation of angiogenic-linked genes (Figure 1) [18].

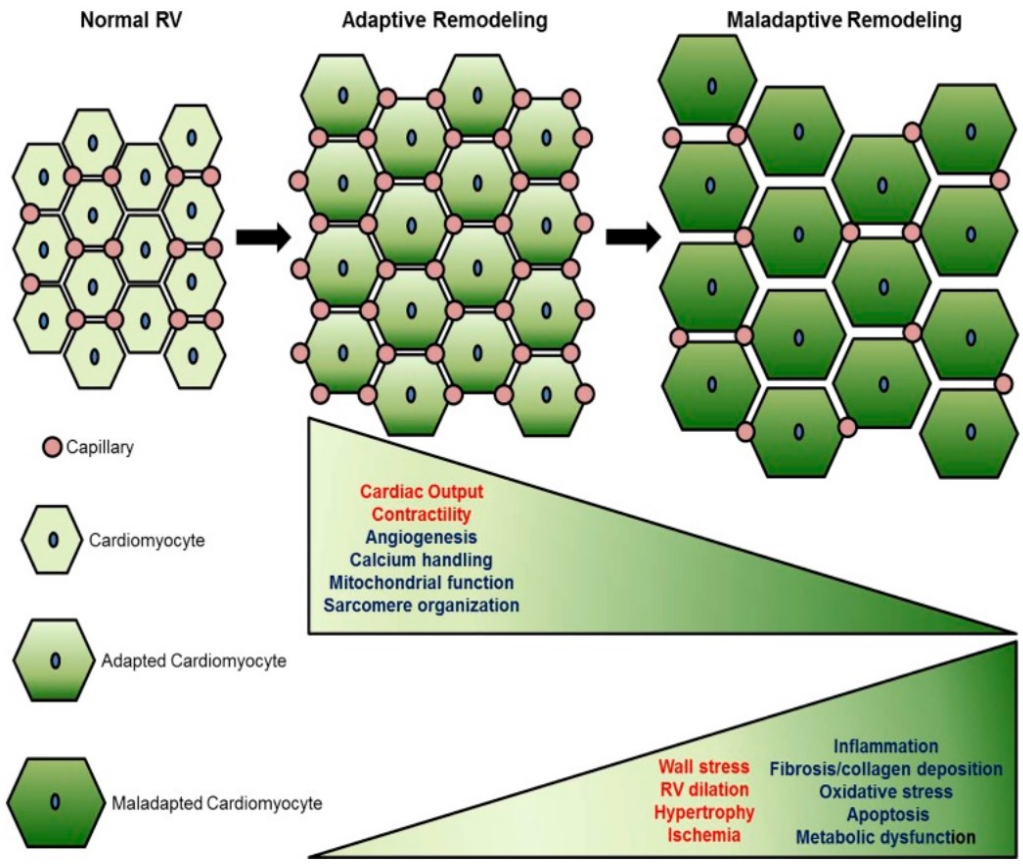

Figure 1. Representative schematic showing different capillary to cardiomyocyte proportions under normal, adaptive (compensated), and mal-adaptive (decompensated) remodeling. Disproportionate changes result in reduced CO and contractility. Structural changes that accompany disproportionate growth include RV chamber dilation and cardiomyocyte hypertrophy. This image was taken, with permission, from Frump et al. (2018) [15].

1.2.2 Current therapies for PAH

Therapeutic options for patients with PAH are focused on addressing manifestations of PAH to provide comfort for patients. Given the unique complexity of PAH, many of the treatment options for the other types of PH (Groups 2-5) are not effective for PAH patients. The field is still searching for treatment strategies that act to reverse the consequent remodeling associated with chronic pressure overload seen in PAH patients. Current therapies, that mainly act by producing pulmonary vasodilation, can slow the progression of the diseases; however, PAH remains incurable and novel therapeutic options are needed to improve patient outcomes.

1.2.2.1 Vasodilators

Endogenous lipid molecule from the eicosanoid family, prostacyclin (PGI_2), is produced by endothelial cells (EC) from arachidonic acid via prostacyclin synthase. PGI_2 exhibits vasodilatory effects on the vascular bed by causing smooth muscle relaxation [19]. PGI_2 has also shown anti-proliferative effects [19]. PGI_2 analogues have been synthesized and used for PAH therapies; accepted analogues include Epoprostenol and Treprostinil. Highly selective prostacyclin receptor agonists, such as Selexipag, have also been used as a PGI_2 analogue for PAH treatment [20]. Most notably, a clinical trial in 2015 found that Selexipag administration in PAH patients significantly reduced the risk of mortality compared to placebo [21].

Another compound that has showed efficacy is nitric oxide (NO). NO is a vasodilator that regulates vessel tone in the pulmonary circulation by stimulating a cascade that leads to cyclic guanosine monophosphate (cGMP) release, inducing relaxation of

smooth muscle cells (SMC) [11]. NO produced is reliant upon NO synthase (NOS). There is evidence emphasizing the relevance of the NO pathway as a potential target for PAH therapies [22]. Current therapies for PAH patients related to the NO pathway include phosphodiesterase-5 inhibitors (PDE-5i) which prevent cGMP degradation. Clinically approved forms of PDE-5i include sildenafil (sold under brand name "Viagra"), and tadalafil [23], [24].

There is also a cohort of PAH patients recognized as "long-term responders to calcium channel blockers (CCB)" who are classified as PAH patients that exhibit vasodilation and relaxation of the vasculature tone and show unchanged or improved hemodynamics after one year when treated with CCB alone [24]. A main concern of these vasodilator agents is their efficacy and safety for PAH patients when used long-term [25]. Patients with long-term responsiveness to CCB exhibit distinct molecular signatures in lung fibroblasts that differentiate them from non-long-term responders to CCB. Patients who are responsive to long-term CCB display better long-term survival compared to non-responsive patients [24].

1.2.2.2 Endothelin Receptor antagonists

The innermost layer of pulmonary arteries comprised of pulmonary endothelium. The pulmonary endothelium is responsible for the management of vascular structure and function through the delivery of endothelial-derived vasoactive factors, like endothelin-1 (ET-1) [26]. In the nineties, it was discovered that ET-1 levels were elevated in PH patients [27]. Since the discovery, ET-1 receptor antagonists have been adopted as potential treatment agents for PAH. ET-1 acts as a vasoconstrictor by stimulating contraction of

pulmonary vascular SMC through ET_A or ET_B receptors [28]. Both ET_A and ET_B receptors are populated on the outer membrane of the pulmonary artery SMC; they mediate vasoconstriction through regulation of intracellular calcium levels [29], [30]. Additionally, ET_B receptors are found on the membrane of pulmonary ECs and control the EC release of vasodilators like PGI_2 and NO [31]. ET-1 receptor antagonists that have been approved for PAH patients include bosentan, an ET_A and ET_B receptor antagonist, and ambrisentan, a highly selective ET_A receptor antagonist [23].

1.2.3 Experimental models of PAH

The establishment of experimental models have been critical in the pursuit of understanding the pathophysiology of PAH and associated RV remodeling and supporting the translation to a clinical setting. While there are various developed models of PAH in different animal species, many of these models only partially represent the pathological characteristics of human PAH. The majority of animal PAH research has relied upon rat models because rats have shown better susceptibility to disease development in response to mode of model development [32]. The two most utilized rat models to recreate PAH *in-vivo* are the monocrotaline (MCT) model and the Sugen-Chronic hypoxia (SU/Hx) model of severe PAH [32], [33]. There are other rat models of PAH that could be used, such as chronic hypoxia model, however, this model is better suited to study Group 3 PH (PH due to lung diseases and/or hypoxia) [33]. Considering the relevance to the focus of this thesis, discussion of the experimental models will be limited to those that best reproduce the clinical manifestations and pathophysiology of PAH. For in-depth review of other experimental models of PH, please refer to article by Ryan et al. [33].

1.2.3.1 The MCT Rat Model

In 1961, it was discovered that rats develop pulmonary vasculitis after being fed *crotalaria spectabilis* seeds that contained a plant alkaloid, MCT [34], [35]. In follow-up studies, MCT-fed rats went on to develop RV hypertrophy, increased right ventricular systolic pressure (RVSP), and medial thickening of the pulmonary arteries [36]. It was discovered that MCT has active pyrrolic derivatives once metabolized by cytochrome-P450 enzymes [35]. The active pyrrolic derivatives possess the ability to cause EC injury [36]. With these findings, a reliable and reproducible MCT model of PAH was established in 1967 [36].

The simplicity and feasibility of the MCT model are primary reasons why it is so widely utilized in PAH research today. A single administration of MCT (60-100 mg/kg, subcutaneously) is sufficient to lead to PAH within 3-4 weeks, with high rates of mortality observed 5-8 weeks post administration [37]. MCT exhibits a dose-dependent response, as lower doses (20 mg/kg) result in mild cases of PAH which are nonlethal and futile when severe PAH is the goal [38]. Considering that the MCT model is a relatively acute model, there is no time for significant adaptive remodeling to take place. Rather, the elevated RVSP and RV hypertrophy progress into eventual RV failure [38].

As previously mentioned, MCT is converted into an active pyrrolic metabolite by the cytochrome P-450 enzyme CYP3A4 [33]. The active metabolite initiates toxic effects on the pulmonary endothelium such as DNA damage, impairments in the NO signalling pathways, and activation of various proliferation cascade [33]. Various MCT studies have observed upregulation in reactive oxygen species (ROS) in the lungs [39]. Within 10 days of MCT administration, SMC proliferation in small PA has been observed.

Muscularization of pulmonary precapillary arterioles is evident approximately two weeks post MCT administration. SMC proliferation in this model leads to medial wall thickening and increased PVR [33]. Consequently, the mean PAP in MCT rats is elevated to more than 35 mmHg by 4-6 weeks post MCT administration, followed by right ventricular hypertrophy (RVH) [40].

The MCT model, is not without its drawbacks; namely, the MCT rat model lacks plexiform lesions, structures that emerge and consist of fibrotic tissue that block arteries, a key histological feature that has been observed in human PAH patients [41]. Additionally, the effects that the active MCT metabolite exerts are not specific to the pulmonary circulation. Considering the off-target effects of MCT coupled with the time required for severe PAH to develop, long-term survival is poor and animal mortality, at higher doses of MCT, may be unrelated to PAH [32]. Apart from these limitations, MCT model reproduces many features of human PAH such as increased RVSP, changes in cardiac function and structure that are later described in detail. Additionally, the model does not require specific setup for experiments. Moreover, this model does not include exposure to hypoxia, which makes this a relevant model to study group-1 PH. The MCT model has been instrumental in developing our understanding of the mechanisms of PAH pathophysiology and present-day treatment options.

1.2.3.2 The SU/Hx Rat Model

The SU/Hx model combines the administration of Sugen-5416 (Sugen, SU-5416), an inhibitor of vascular endothelial growth factor receptor 2 (VEGFR-2) with chronic hypoxia. Sugen was developed as an anticancer drug with common name semaxinib [40].

The SU/Hx model induces PAH in rats via a single dose of Sugen injected subcutaneously in combination with three weeks exposure to hypoxia (10% O_2) followed by return to normoxia for 2-9 weeks [42]. Based off studies investigating the role of vascular endothelial growth factor (VEGF) in the progression of PAH, it was hypothesized that the inhibition of VEGF-2 would prevent the development of PAH. Researchers chose Sugen to inhibit VEGF receptors, such as VEGFR-2, as Sugen is highly selective and potent [43]. Rather than being beneficial towards preventing PAH, researchers discovered that inhibition of VEGFR-2 resulted in progressive PH and RVH [40]. Capillary obliteration and substantial EC proliferation were observed under this model [40]. The pathohistological characteristics of the SU/Hx model have been found to be identical to the clinical hallmarks seen in human PAH patients [42]. Despite achieving higher pressures under the SU/Hx model compared to the MCT model, the SU/Hx model has a much lower mortality [33]. The low mortality in addition to the ease with which human PAH features can be replicated makes the SU/Hx model a highly favoured model in PAH research [33]. This model is not without its limitations; a specific setup requiring an expensive hypoxia system to house animals is required. Animals are not to be taken out of hypoxic conditions during the three-week period. This model is also not a sole representation of group 1 PH; due to the utilization of hypoxia, this model is an overall representation of a mix between groups 1 and 3 PH [33].

1.2.3.3 Other models used to study PAH

There are other animal models that have been used to a lesser extent to study PAH, although, as mentioned earlier, they are likely models that most appropriately produce Group 3 PH. Nonetheless, they will be briefly described.

The chronic hypoxia model is often utilized as a method to model Group 1 PH despite animal mortality being unrelated to RV failure. The chronic hypoxia model produces very mild PH and demonstrate less pulmonary vascular remodeling and RVH compared to that seen in the MCT or SU/Hx models.

The pneumonectomy model, a removal of one of the lungs, has also been used in PH animal studies. A reduction in the pulmonary vasculature by 50% increases the demands of the remaining pulmonary arteries and microvasculature. The pneumonectomy has been more utilized in combination with MCT or Sugen [33]. When MCT is combined with a pneumonectomy, the mean PAPs are increased even greater than what has been observed with MCT only [33]. This model is created by performing the pneumonectomy and then administering MCT (typically 60mg/kg) one-week post-surgery. Histological findings are more severe in this model, and even produce plexiform-like lesions, which the MCT model alone does not produce [33]. Despite the findings that the pneumonectomy + MCT model yield, this model, like most surgically invasive models, is associated with high animal mortality and morbidity.

1.2.4 Mortality in PAH patients

Generally, PH diagnosis and death has increased in recent years, specifically in women and adults [44]. According to the NHLBI Primary Pulmonary Hypertension

Registry, most PAH patients die from progressive right heart failure (RHF) [44], [45]. There are still gaps in understanding what the modes of death are in PAH patients, despite advancements in diagnosis. In a cross-sectional study by Tonelli et al, data were collected as part of a project to improve quality of life and was later approved by the Institutional Review Board at the Cleveland Clinic [46]. The authors collected data from patients over a four-year period, 2008-2012, and included data from deceased PAH patients that had regularly documented clinical visits. Their findings showed that 73% of patient mortality was accredited to right ventricular failure or sudden cardiac death [46]. Another study that focused on PAH emergency treatments found that sudden cardiac death was a potential cause of nearly 50% of patient mortality [45]. Overall, RHF is the primary cause of death in PAH patients; however, approximately 50% of patients die from other causes.

1.2.5 Arrhythmias and electrical remodeling in PAH

In the late 1970s, a study found that over 70% of PAH patient electrocardiogram (ECG) displayed sinus tachycardia, sinus bradycardia, or AV block [48]. The chronic pressure overload that leads to right heart remodeling generates substrates that, in left-heart studies, have been found to be arrhythmogenic [48]. Factors that lead to the generation of such substrates include, but are not limited to:

1. Autonomic nervous system (ANS) modulation: PAH patients have been noted to present with high frequency ventricular ectopy, reduced HR variability, elevated levels of norepinephrine, and selective downregulation of beta-adrenergic receptors in the RV [49]. These are indicators of increased sympathetic activity in the RV. Chronic increases in pulmonary pressure

combined with a decline in cardiac function could result in changes to the ANS that leads to an overall increase in sympathetic activity. These changes are described as “pro-arrhythmic”, as these characteristics contribute to events of dysregulation that could potentially lead to an altered electrophysiological state, both acutely and chronically [49].

2. Delayed cardiac repolarization: QT dispersion is a hallmark precursor of arrhythmias and predictor of mortality [50]. A study comprised of severe PAH patients found mean QTc (corrected) prolongation, however the mechanisms underlying interval prolongation in relation to an increase predisposition towards cardiac arrhythmias has not been described [50]. Impaired cardiac electrical activity has been linked to the structural remodeling that occurs during PAH progression [51]. Over time, the multi-faceted mal-adaptive remodeling results in chronic changes to the electrical activity, referred to as electrical remodeling.
3. Alteration to action potential duration (APD): APD is tightly regulated and shortening or prolongation of APD can lead to cardiac arrhythmias. Prolongation of APD has been linked to left sided heart failure [52]. Specifically, prolongation of APD has been linked to early after depolarization (EAD) and arrhythmias. EADs have been linked back to increased myocardial fibrosis and increased Ca^{2+} levels in the cytosol, ultimately reducing the repolarization reserve [53].
4. RV myocardial ischemia: ischemia has been proposed as a mechanism that produces arrhythmogenic substrates in PAH patients such as calcium overload

and scar tissue. The factors that lead to overall arrhythmogenicity is still up for discussion and could be caused by intra-myocardial arteriolar compromise, inadequate coronary perfusion, and increased myocardial oxygen demand [47].

5. RV Fibrosis: Fibrosis refers to excessive extracellular matrix deposition that can interfere with conduction and may act as an arrhythmogenic substrate [54]. RV remodeling associated with PAH has been linked to increased fibrosis [55]. Considering that the structural remodeling associated with PAH includes increased fibrosis coupled with the acknowledgement that fibrosis impairs electrical conduction, it is probable that fibrosis may contribute to arrhythmias.

There are published studies that investigate electrical remodeling and arrhythmias in animal models of PAH [51], [56]. Previous studies have investigated electrical remodeling in PAH using the MCT and Sugen/pneumonectomy animal models, respectively [51], [56]. Despite significant findings of electrical remodeling, which will be mentioned in later sections, previous studies are limited in their relevance to a PAH cohort that is extremely vulnerable to sudden cardiac death. The strain of rat used in previous studies, Sprague-Dawley (SD), has been reported to show better survival and develop a more progressive PAH compared to the Fischer CDF rat strain (used in this project) [57]. Fischer CDF rats are more susceptible to developing severe RV remodeling and sudden death. Therefore, Fischer CDF rats may be better suited to study m3echanisms of sudden death in PAH.

CHAPTER 2: OBJECTIVES AND HYPOTHESIS

PAH is a progressive incurable disease, with unclear etiology and a poor 5-year transplant free survival rate of only ~55%. RHF, occurring as a direct consequence of increased right ventricular afterload, is the primary cause of death of PAH patients; however, in some studies approximately 50% of patients die from other causes. Evidence suggests that one such cause is cardiac arrhythmias, which contribute to symptom burden, morbidity, in-hospital mortality, and can result in sudden death. Currently, very limited preclinical studies have investigated the cardiac arrhythmias and underlying mechanisms in PAH. Therefore, the overall objective of this thesis was to begin the studies investigating the mechanisms of increased susceptibility to cardiac arrhythmias in a model of severe PAH that shows high susceptibility to sudden death.

2.1 Objectives

1. To establish the Fischer CDF rat MCT model of severe PAH to study its features, characteristics, and sudden cardiac death.
2. To establish an experimental protocol to explore electrophysiology with optical mapping in the Fischer CDF rats MCT model of severe PAH.
3. To explore changes in electrophysiological parameters during the progression of PAH in the Fischer CDF rats MCT model of severe PAH.
4. Studying susceptibility to spontaneous arrhythmias and in response to pacing

2.2 Hypothesis

Severe PAH in Fischer CDF rats exposed to MCT increases susceptibility to cardiac arrhythmias, and thereby susceptibility to sudden death, due to electrical remodeling and reduced vascular density.

CHAPTER 3: MATERIALS AND METHODOLOGY

Contributions:

Hemodynamic measurements, heart isolation and perfusion were completed by Dr. Ketul R. Chaudhary. MCT injections and echocardiography were completed by Dr. Ketul R. Chaudhary and Tony El-Rabahi. Optical mapping, histology, and all analyses were completed by Tony El-Rabahi.

3.1 Animal Care and Handling

All animal procedures were approved by the University Committee on Laboratory Animals (UCLA) of Dalhousie University and were in accordance with the Canadian Council on Animal Care (CCAC) guidelines. Male Fischer CDF rats (aged 6-9 weeks) were obtained from Charles River Laboratory (Montreal, QC, Canada). Upon arrival to the Carleton Animal Care Facility (CACF), animals were given at least one week to acclimatize before any procedure. Throughout the duration of the studies, animals were housed and maintained on a light-dark (12 hours/12 hours) cycle and had access to food and water ad libitum. Mashed food and diet gel were provided as enrichment for all groups.

3.2 Experimental Design Overview

To study the susceptibility to cardiac arrhythmias in PAH, the Fischer CDF rat monocrotaline (MCT) model was utilized. Rats were randomly assigned to the following groups: control, 4-weeks post-MCT (MCT-4), and 5-weeks post-MCT (MCT-5). At the end of the study, echocardiography and electrocardiography were performed, followed by hemodynamic measurement, isolated heart perfusion, and optical mapping. Hearts were then collected, the atria were removed, and the RV was separated from the LV and septum (LV+S). Weights of RV and LV+S were recorded, and the heart samples were placed in 4% paraformaldehyde (PFA) and processed for histology. Procedures were completed within ± 1 day of anticipated end date. Procedures for all measurements, sample preparation, and analyses are described below.

3.3 Experimental Groups

This study had 2 experimental groups and a control group to study the effects of PAH on electrical remodelling and potential susceptibility to arrhythmia.

Control (n=5): These animals did not receive any treatment (naïve) and were used after the acclimatization period. Animals were between the ages of 10-11 weeks at euthanasia. Initial sample size for this group was n=11, however, not all data was captured reliably due to technical challenges related to collection of optical mapping data or use of dye.

MCT-4 (n=9): This group was injected with MCT (60 mg/kg, s.c.) and end-study was performed 4 weeks after MCT injection. Once experimental endpoint had been achieved ± 1 day, animals were used for intended study purposes. The initial sample size for this group was 13, however, some animals were excluded from this study due to technical challenges related to quality of optical mapping images. Two animals from this group reached humane endpoint before the 4-week timepoint, and thus were excluded.

MCT-5 (n=5): This group was injected with MCT (60 mg/kg, s.c.) and end-study was performed 5 weeks after MCT injection. Once experimental endpoint had been achieved ± 1 day, animals were used for intended study purposes. The initial sample size for this group was 11, however, three animals were not included due to animals reaching humane endpoint prior to the 5-week timepoint. Additionally, there were technical challenges with the experimental setup that caused loss of capture or unsuccessful experiments.

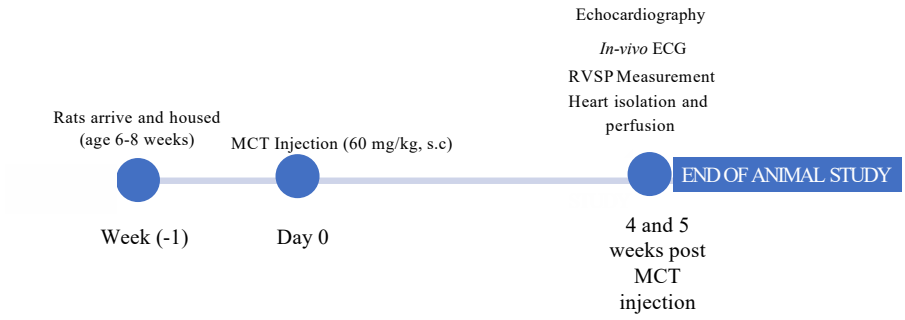

Figure 2. Timeline of Fischer CDF MCT model and following procedures.

3.4 Monocrotaline Preparation and Injection

Preparation: Monocrotaline (160 mg, C2401, Sigma-Aldrich, USA) was dissolved in 1mL of sterile 1M hydrochloric acid (HCl) (prepared in lab) and 4mL of sterile water (Bexter, USA) was added to the solution. Using 1M sodium hydroxide (NaOH) (SS255-1, Fisher Health Care, TX, USA), the pH of the solution was adjusted to 7.4. Final volume was adjusted to 8mL with sterile water (Bexter, USA) and the final solution was filtered through a 0.22µm filter in a biosafety cabinet. The MCT solution was made fresh on day of injection.

Injection: Animals were numbered, and body weights were measured. Volumes of MCT solution were calculated in accordance with animal body weights to achieve a dose of 60 mg MCT /kg body weight. A single dose of MCT was injected s.c. using a 26-gauge needle and 1mL syringe into the dorsal flank of the rat. Subcutaneous injection was chosen over intra-peritoneal to avoid any internal organ damage, as both methods of administration produce the same phenotype.

Following MCT injection, rats were maintained at room-air for 4 or 5 weeks (MCT-4 and MCT-5, respectively) and echocardiography, electrocardiography, hemodynamic measurement, isolated heart perfusion, and sample collection were performed as described below. During the experiment, animal health was closely monitored. Any animal meeting the criteria for humane endpoint was taken for data collection and euthanized immediately. Animals were considered at humane endpoint if lost more than 15% of body weight from maximum weight. In absence of more than 15% body weight loss from maximum weight, animals were considered at humane endpoint if an animal lost more than 5% overnight weight together with M1-M2 respiratory distress and at least two of the following: notable porphyrin staining (nose/eyes), hunch, grimace, quiet behavior, pale/blue/cold extremities (feet, nose, ears, tail), weak/unable to grip top of cage, piloerection.

3.5 Echocardiography

On the day of experimental endpoint, RV structure and function were assessed using non-invasive transthoracic echocardiography (Vevo2100, VisualSonics, NY, USA). Animals were anesthetized by isoflurane inhalation (5% isoflurane, 1 L/min O_2) using an induction chamber. Rats were removed from chamber and placed on a heated pad (37°C) with the nose placed into a nose cone supplied with isoflurane (1.5-2% isoflurane, 1L/min O_2). Animal eyes were treated with petroleum-based ophthalmic ointment. The chest was prepared via shaving and Nair hair removal gel. After preparation, chest was cleaned with distilled water. Warm ultrasound gel was applied on the chest area and images were acquired while the animals were anesthetized.

The aorta was located using a parasternal long axis view. To capture the PA, the transducer was rotated clockwise from the position viewing the aorta. B-mode images were captured for PA diameter. Pulse wave doppler mode was used to measure PA velocity-time integral (PA-VTI). Stroke volume (SV) (Equation 1) and cardiac output (Equation 2) were estimated using PA diameter, PA-VTI, and heart rate (HR), according to a previously described method [18]. To determine the pulmonary arterial acceleration time and ejection time (PAAT and PET, respectively), PAAT was measured as the time from the initiation of systole to peak outflow velocity (Fig. 3B). PET was measured as the time from the initiation of ejection to the end of ejection (Fig. 3B). Using a parasternal short axis view (M-mode), images for structural measurements of the right and left ventricles (i.e. diastolic RV internal diameter, RVIDd; diastolic left ventricular internal diameter, LVIDd; RV free-wall thickness RVfWT; and fractional shortening, FS) and HR were acquired (Equation 3, Fig. 3A). Apical four chamber view (B-mode) was used to evaluate RV chamber area during diastole and systole to measure fractional area change (FAC) (Equation 4, Fig 3C-D). The RV chamber area during diastole and systole from consecutive cardiac contractions were traced from B-mode images. From there, RV area during diastole (RVAd) and systole (RVAs) were calculated. Following echocardiography, electrocardiography was performed.

Equation 1: $SV = \pi \left(\frac{PA\ Diameter}{2}\right)^2 x\ VTI$

Equation 2: $CO = SV\ x\ HR$

Equation 3: $FS = (RVIDd - RVIDs)/RVIDd$

Equation 4: $FAC = (RVAd - RVAs)/\ RVAd$

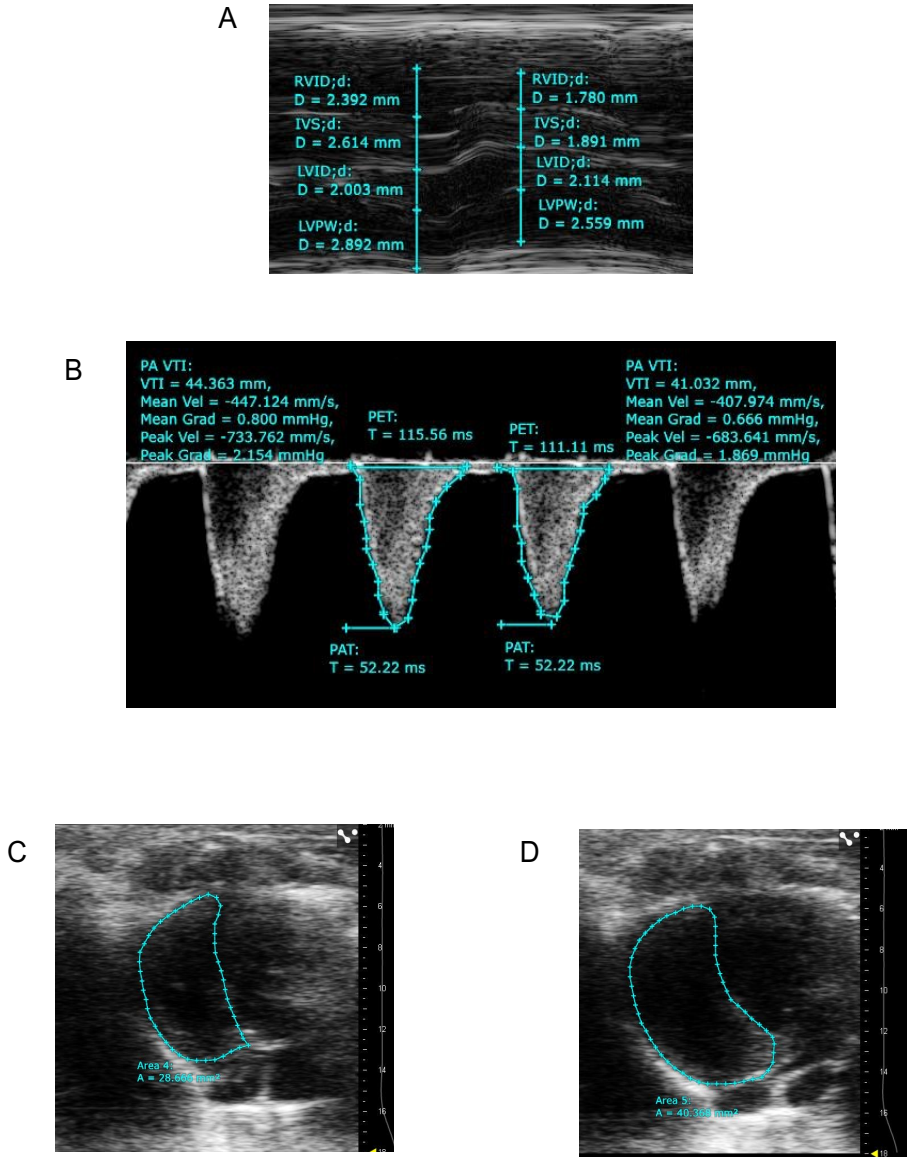

Figure 3. Representative end-point echocardiography images. (A) M-mode image, (B) Pulse-Wave doppler image of pulmonary arterial blood flow, (C-D) B-mode image capturing area of RV. (A,C-D) measurements were taken for consecutive contraction (C) and relaxation (D), respectively. RVID, right ventricular internal diameter; IVS, inter-ventricular septum; LVID, left ventricular internal diameter; LVPW, left ventricular posterior wall**;** PA VTI, pulmonary artery velocity time integral; PAT, pulmonary acceleration time; PET, pulmonary ejection time; Vel, velocity; Grad, gradient.

3.6 Electrocardiography

Post echocardiography, animals were kept at 1.5-2% isoflurane. Negative (right shoulder), positive (left leg), and ground leads (left shoulder) were placed on the rat in lead II position. ECG was recorded for 3-4 minutes and analyzed using LabChart 8 (ADInstruments-North America, CO, USA). Following ECG, rats were placed in a recovery cage and later transported to another room for catheterization.

3.7 RV Catheterization

To determine endpoint measurements of RVSP, RV catheterization was conducted. RVSP was measured using a 3F high-fidelity pressure catheter (Transonic-Scisense Inc., ON, Canada). Under anesthesia, the right jugular vein was exposed, and the pressure catheter was advanced through the superior vena cava into the RV. Catheter placement was confirmed by observing pressure tracings prior to collection of data. Hemodynamic parameters were recorded and analyzed using LabChart-8 (ADInstruments-North America, CO, USA).

3.8 Heart Isolation and Langendorff Perfusion

Immediately following RVSP measurements, the abdominal cavity was surgically opened, and the rats were euthanized via exsanguination by dissecting the abdominal aorta. The open abdominal cavity was physically expanded using sharp blunt-end scissors and the diaphragm was cut to reveal the heart and lungs. The thoracic cavity was further exposed until the aortic arch was visible. Surgical scissors were slid behind the heart to separate any fibrous attachments. The heart was excised at the aortic arch, and the aorta

was cannulated and retrogradely perfused at a rate of 6 mL/min with Krebs-Heinselet solution (containing [in mM]: 120 NaCl ; 4.7 KCl ; 24 $NaHCO_3$; 1.4 NaH_2PO_4 ; 1.0 $MgCl_2$; 1.8 $CaCl_2$; 10 Glucose ; osmolality: 300 ± 5 mOsm/kg ; pH: 7.4 ± 0.04) bubbled with carbogen (95% O_2, 5% CO_2) on a Langendorff perfusion apparatus (Fig. 4). During retrograde heart perfusion, the perfusion buffer flows down the aorta, opposite to the regular physiologic flow of blood. Under pressure, the aortic valve is closed, and the perfusion buffer can supply the coronary arterial vasculature via the left and right aortic sinuses. In this way the capillary beds are filled, with the perfusion buffer leaving the heart via the coronary veins, eventually to be collected in the coronary sinus and the right atrium [58]. Once isolated hearts were setup on the Langendorff apparatus, both ECG and pacing leads were placed on the heart. ECG leads were placed in two distinct locations, on opposite ends of the heart (atria and left ventricle). Bipolar pacing leads were placed on the RA and RV.

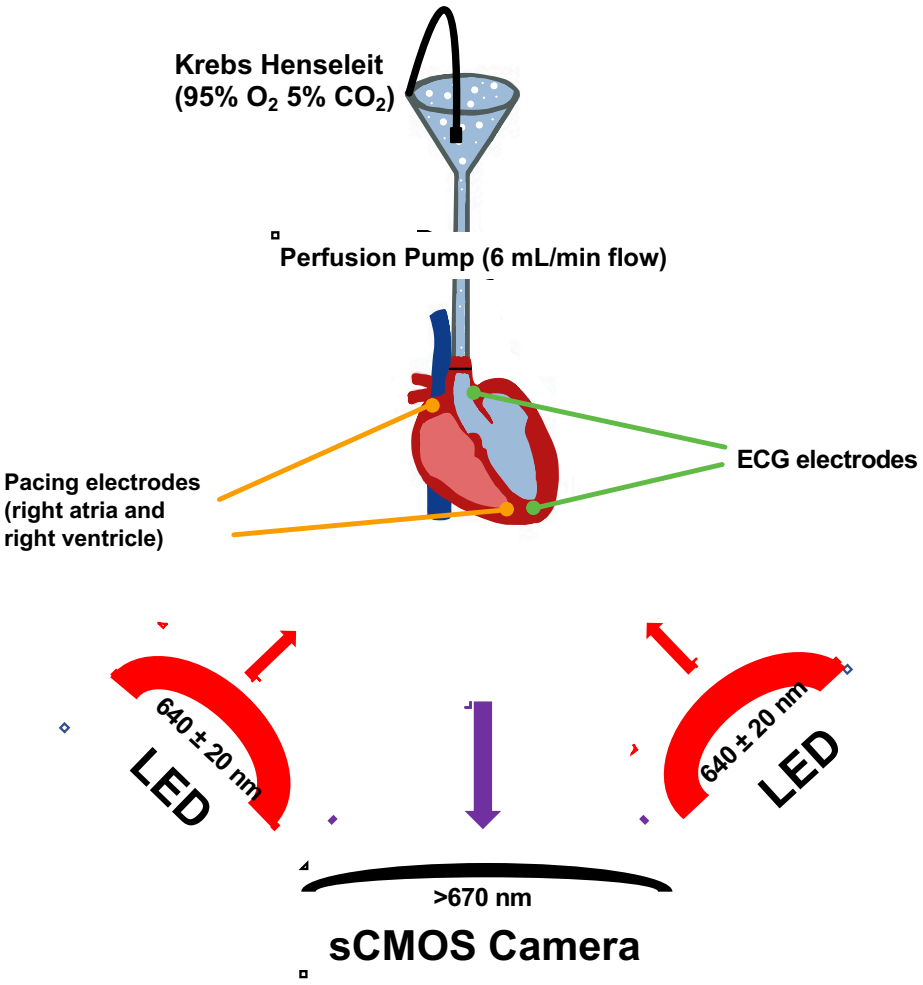

Figure 4. Schematic of experimental setup using Langendorff apparatus. Cannulation of the aorta allowed for retrograde perfusion at a constant flow rate of 6 mL/min of Krebs-Henseleit physiologic buffer, oxygenated using a carbogen mixture (95% O_2 5% CO_2).

3.9 Voltage Optical Mapping

Once isolated and heart perfusion was established, hearts were loaded with a voltage-sensitive dye (di-4-ANBDQPQ: D41633, Toronto Research Chemicals, ON, CAN) by direct injection into the aortic cannula (10µL bolus of 27 mM, later 9 mM, solution in absolute ethanol, delivered in 0.4 µL increments over 2-3 minutes). As shown in Figure 5, the dye was excited using two red light emitting diodes (PT-121-R, Luminus Devices, CA, USA) with a band-pass filter (640 ± 10nm) (640/20, Chroma Technologies, VA, USA). Dye excitation results in fluorescent emission, whose spectrum shifts with changes in membrane potential [59]. Emitted fluorescence was collected at 500 frames/sec using a 350 x 512-pixel sCMOS camera (Zyla, Andor Technology, Belfast, UK) through a 17 mm high-speed lens (DO-1795, Navitar, NY, USA) at 44 µm/pixel and a long-pass filter (>670 nm) (670LP, Chroma Technologies, VA, USA).

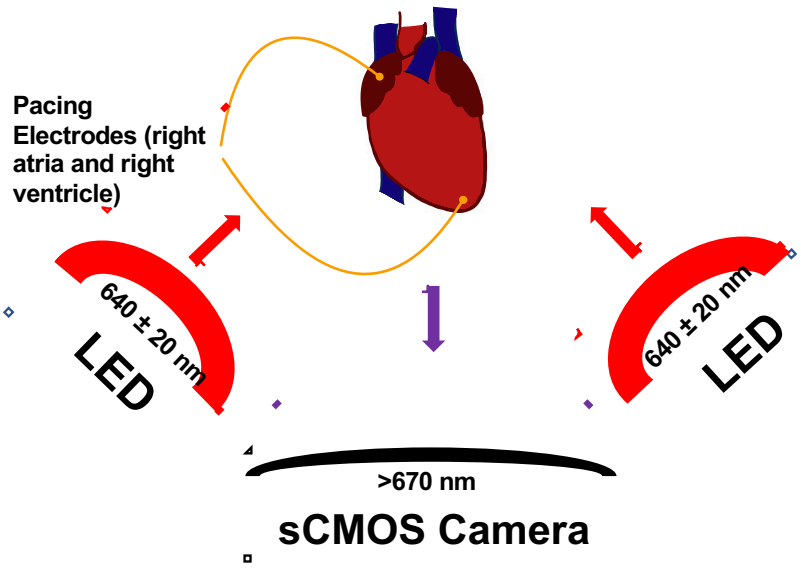

Figure 5. Schematic of optical mapping of the right side of the heart. A voltage-sensitive dye (di-4-ANBDQPQ) was perfused into the tissue. Excitation with red LED lights (640 ± 20 nm) causes the dye to fluoresce near the infrared wavelength range. Epicardial fluorescence was captured using sCMOS camera with a 670 nm long-pass filter.

3.10 Experimental Protocol: Atrial and Ventricular Pacing

To capture recordings for optical mapping analysis, 10 μM (+/-)-Blebbistatin (B592490, Toronto Research Chemicals, ON, CAN), a myosin-II inhibitor, was administered into the perfusate to block mechanical contraction of the heart. At the same time, the voltage sensitive dye was administered as described above. A 10-minute period was given to allow (+/-)-Blebbistatin to reach the cardiac tissue and for the hearts' activity to normalize on the perfusion apparatus. Once mechanical contraction of the hearts had stopped, a baseline recording was taken. Afterwards, the pacing protocol was initiated and conducted manually as follows (Fig. 6):

> The heart was paced at 5.55 Hz from the right atria for 60 seconds. A recording of the first 15 seconds of pacing was taken and saved for analysis. Once 60 seconds had passed, the heart was then immediately paced at 5.55 Hz from the right ventricle for 60 seconds. A recording of the first 15 seconds of the ventricular pacing was saved for analysis. Once 60 seconds of ventricular pacing had passed, hearts were given 60 seconds to return to baseline activity. Identically, atrial, and ventricular pacing was performed at 8.33 Hz and 16.67 Hz. Once pacing at 16.67 Hz was completed, this concluded a complete "round" of the pacing protocol. Hearts were given 60 seconds to return to baseline, before taking another baseline recording. The pacing protocol was then initiated again, identical to the first "round" of pacing. This pacing protocol was conducted 2-4 times per animal to ensure that sufficient, clean signals were saved for future analyses.

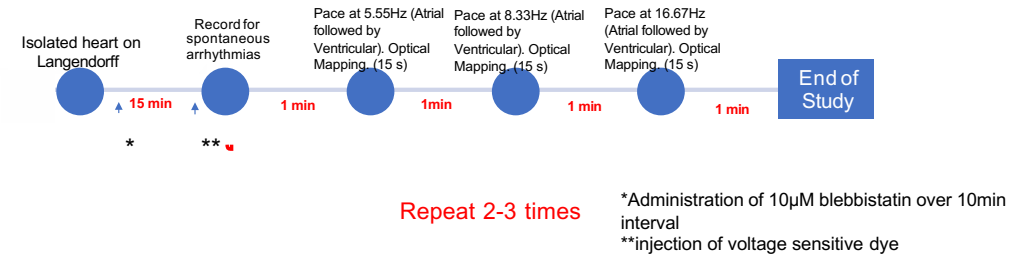

Figure 6. Schematic of atrial and pacing protocol. Recordings were captured as described above.

3.11 Optical Mapping Analysis

To determine if electrical remodelling was present, we analyzed various action potential (AP) parameters over a region in the middle of the right ventricle, including the maximum rate of membrane potential change during the AP upstroke (dF/dt_{max}, in units of normalized fluorescence per millisecond, also coined "upstroke velocity") and APD at 20%, 50%, and 80% repolarization (APD_{20}, APD_{50} and APD_{80}, respectively; calculated as the difference between the time of membrane potential restoration to 20%, 50%, and 80% of resting values and the time of AP activation, set as the point of dF/dt_{max}) (Fig. 7). Conduction velocity (CV) and heterogeneity of repolarization were also analyzed across the RV.

Custom designed programs in MatLab were used for analysis (Quinn Laboratory, Dalhousie University, NS, CAN). A region of interest (ROI) in the middle of the RV was selected and held consistent for all hearts. Fluorescent signals were averaged within each ROI, filtered with a 60 Hz low-pass temporal filter, inverted, and normalized. Values of dF/dt_{max} and APD_{20}, APD_{50}, and APD_{80} were calculated for each action potential and averaged across the values from a 5-10 second sample of each pacing and non-pacing/baseline recording.

To calculate CV across the RV, ventricular pacing recordings were uploaded into MatLab (Quinn Laboratory, Dalhousie University, NS, CAN). The axis of ventricular activation was confirmed, and a line of ROIs was placed across the ventricle, aligned with the axis. CV was calculated as the distance between two ROIs divided by the time between each ROI's activation. Velocities were taken for three individual beats per round of ventricular pacing at 5.55 Hz and compared between control and MCT-5.

APD heterogeneity assesses the dispersion of repolarization across the RV. To compare dispersion, a ROI of the RV was taken during non-pacing and atrial pacing at 5.55 Hz conditions. Signals were filtered with a 60 Hz low-pass temporal filter, an 11-point spatial filter, and inverted. An APD pixel map was then generated. From the map, a heterogeneity index (μ) was calculated for an individual beat (Equation 5), where APD^{95} and APD^{5} represent the 95^{th} and 5^{th} percentile of APD_{80} distribution, respectively, and APD^{50} represents the median of the APD_{80} distribution [60]. Indices for all groups were compared for both baseline / non-pacing and atrial pacing at 5.55 Hz conditions.

Equation 5: $\mu = (APD^{95} - APD^{5}) / APD^{50}$

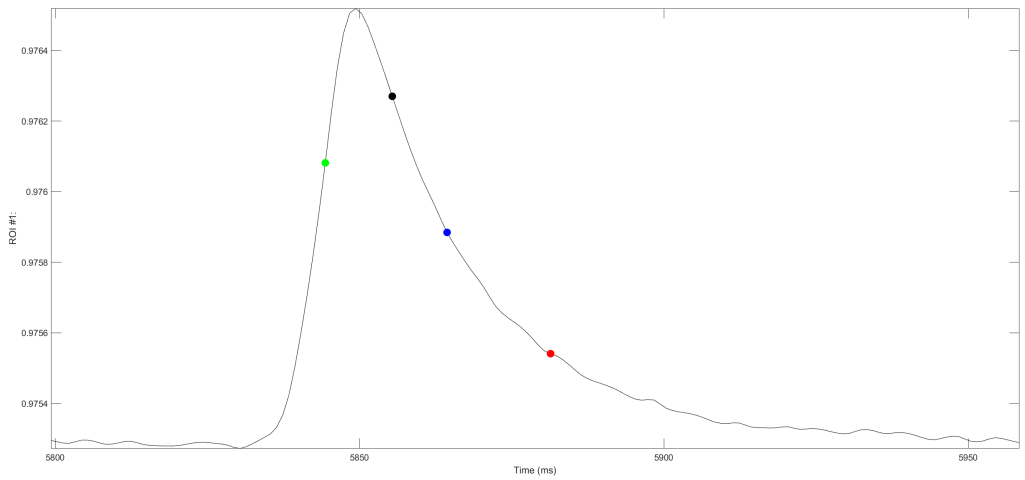

Figure 7. Representative image of MatLab output for 1 signal. Custom designed MatLab programs (Quinn Laboratory, Dalhousie University, NS, CAN) were used to analyze optical mapping recordings. Figure shows the electrophysiological measurements of interest; GREEN, dF/dt_{max}; BLACK, APD_{20}; BLUE, APD_{50}; RED, APD_{80}.

3.12 Assessment of Right Ventricular Hypertrophy

Immediately after optical mapping experiments, the heart was removed from the Langendorff apparatus and the ventricles were surgically dissected from the atria, the aorta, and pulmonary trunk. The hearts were then physically separated into two parts: RV and LV+S. RVH, or the Fulton index, was calculated as RV wet mass divided by LV+S wet mass (Equation 6).

Equation 6: $RVH = \frac{RV}{LV+S}$

3.13 Rat Heart Fixation and Paraffin-embedding

Following weight measurements, the RV and LV+S, were placed in 4% PFA for 48 hours at 4°C followed by a 24-hour wash in PBS. The tissues were then preserved in 70% ethanol until paraffin embedding (Leica EG1160 embedding station, Leica Biosystems Inc., ON, Canada). Using a microtome, 5 µm sections were cut from the paraffin blocks, mounted onto poly-L-lysine coated slides, and dried at 37°C for 16 hours. Fixation, paraffin-embedding, and sectioning was performed by the histology core at Dalhousie University.

3.14 Rat Heart Tissue Sectioning and Histology

The slides were then dewaxed and rehydrated through graded alcohols. Sections were then submerged in xylene three times for 5 minutes each followed by two 2-minute incubations in 100% ethanol. Slides were then submerged in 90% and then 70% ethanol

for 1 minute each, respectively. Slides were then placed in double distilled water for 5 minutes. Following the rehydration procedure, slides were stained using hematoxylin and eosin (H&E), Masson's Trichrome, or immunohistochemistry (IHC) as described below. Following staining, slides were then sealed using Cytoseal media and a coverslip (8312-4, epredia, MI, USA; C2460, UltiDent Scientific, QC, Canada). Slides were left to fully dry overnight prior to any microscopy.

3.14.1 Hematoxylin and Eosin Staining

We conducted H&E staining on the sections of RV collected from control and MCT rats to assess cardiomyocyte cross sectional area (CSA). Sections were stained with the H&E Stain Kit (AB245880, Abcam, MA, USA) as per manufacturer's protocol. Briefly, slides were deparaffinized and incubated in Hematoxylin, Mayer's (Lillie's Modification) for 5 minutes. After two washes of distilled water, sections were incubated in Bluing Reagent for 10-15 seconds. Slides were then rinsed in distilled water and dipped in absolute alcohol (P016EAAN, Greenfield Global, ON, Canada). Slides were then blotted using a KimTech wipe prior to incubation of Eosin Y Solution (Modified Alcoholic) for 2-3 minutes. Slides were finally rinsed in absolute alcohol before being transferred to 70% ethanol, after which dehydration and mounting were conducted.

For H&E analysis, images were taken using an LMI-3000 Series Routine Inverted Microscope (Laxco, WA, USA) at 20X magnification with a SeBaCam Digital Camera (SeBaCam100; Laxco, WA, USA) and SeBaView software (Laxco, WA, USA). Using the freehand selection tool in ImageJ (National Institutes of Health, MA, USA), the perimeters of 20 cells in 3-5 images per ventricle were traced and CSA was calculated (Fig. 8).

Tracings were conducted blinded and were taken from different regions of the sections to limit cardiomyocyte-selection bias. Cardiomyocytes cut cross-sectionally were included in the analysis, whereas sections cut longitudinally or unclearly were excluded. CSA was averaged for cells in each image and then CSA in different images from a single animal was averaged to obtain the CSA for individual animal. CSA was compared between control, MCT-4 and MCT-5.

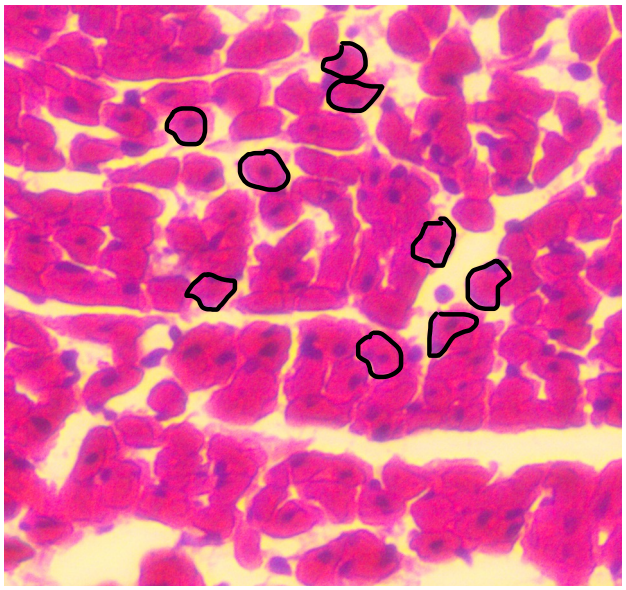

Figure 8. Representative image of Hematoxylin and Eosin staining with examples of cardiomyocytes that would be included in analysis (circled).

3.14.2 Immunohistochemistry

To investigate capillary density, IHC was performed for EC-specific marker, cluster of differentiation 31 (CD31) or platelet endothelial cell adhesion molecule (PECAM-1). Antigen unmasking solution was made using 500 mL of distilled water and 4.9 mL of Citric Acid Based Antigen Unmasking Solution (H-3300-250 Vector Laboratories, CA, USA). It was prewarmed in the microwave for 4 minutes. Deparaffinized slides were then submerged and microwaved on high for 12 minutes. Slides were cooled at room temperature for 10 minutes, followed by a rinse in tap water for 1-2 minutes. Slides were then immediately transferred to a staining jar containing PBS. Sections were washed in PBS buffer for 5 minutes.

Following antigen unmasking, sections were immediately processed for CD31 IHC using Rabbit specific HRP/DAB Detection kit (Abcam-AB64261, MA, USA). Slides were incubated with hydrogen peroxide for 10 minutes and washed four times with PBS with 0.1% Tween™ 20 (PBS-T) for 5 minutes each. Next, non-specific staining was blocked using protein block for 15 minutes. Sections were then washed in PBS-T for 5 minutes. Next, the rabbit polyclonal antibody against CD31/PECAM-1 (NB100-2284, Novus Biologicals LLC, CO, USA) was used at 1:100 concentration with 2% BSA-PBS and incubated for 1 hour at room temperature in a humidification chamber. Slides were then washed in PBS-T four times for 5 minutes each and incubated with Biotinylated Goat Anti-Polyvalent at room temperature for 15 minutes, followed by four washes in PBS-T for 5 minutes each. Sections were then incubated with Streptavidin Peroxidase for 15 minutes, followed by another four washes for 5 minutes each. 3-3'Diaminobenzidine (DAB) chromogen was diluted with DAB Substrate (1:50 dilution) in restricted light conditions

and applied to the sections. Application of DAB produces a brown colour when oxidized by hydrogen peroxide in the presence of peroxidase. Sections were incubated with DAB solution for 10 minutes. Slides were then washed in PBS-T four times for 5 minutes each, dehydrated, and mounted as described above.

For IHC analysis, images were taken using an LMI-3000 Series Routine Inverted Microscope (Laxco, WA, USA) at 20X magnification with a SeBaCam Digital Camera (SeBaCam100; Laxco, WA, USA) and SeBaView software (Laxco, WA, USA). Using the freehand selection tool in ImageJ (National Institutes of Health, MA, USA), the area of the slide occupied by tissue was traced to calculate area. Using the counter tool, blood vessels (stained brown) were counted (Fig. 9). Vascular density was calculated as the quotient of vessel count divided by the tissue area (mm^2).

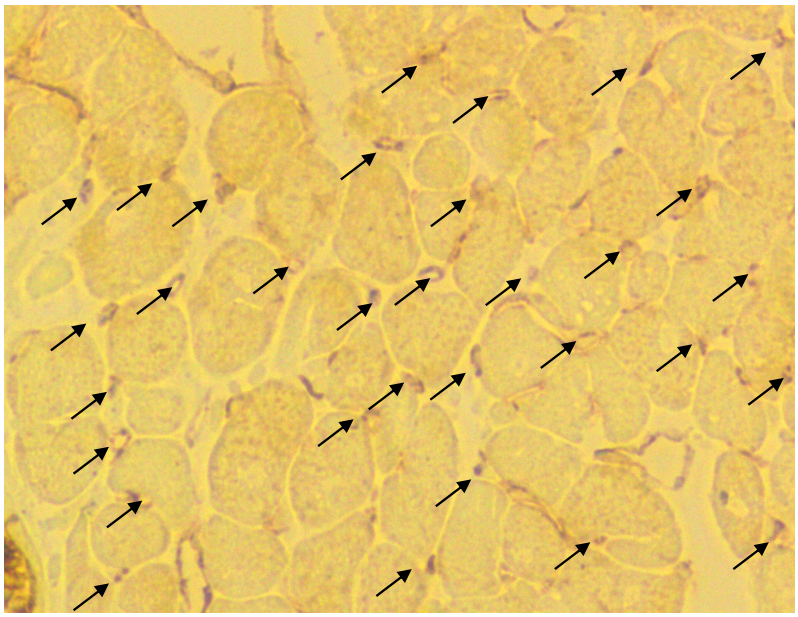

Figure 9. Representative image of IHC staining for CD31 and quantitative analysis.

3.14.3 Masson's Trichrome Staining

To investigate collagen content as a measure of fibrosis in the control and MCT groups, Masson's Trichrome staining was performed. Rat heart sections were rehydrated and prepared as described above and rinsed in running tap water. The Polysciences Masson's Trichrome Stain Kit (25088, Polysciences Inc., Warrington, PA, USA) was used to conduct this staining. Bouin's Fixative was preheated to 60°C and slides were incubated with the fixative for 1 hour. Sections were then washed in running tap water for 5 minutes, followed by a rinse in distilled water. Slides were then incubated in Biebrich Scarlet-Acid Fuchsin Solution for 5 minutes and rinsed in distilled water. Next, slides were incubated with phosphotungstic/phosphomolybdic acid for 10 minutes, drained, and then transferred to an incubation with Aniline Blue for 5 minutes. Sections were then rinsed in distilled water three times before being transferred to 1% acetic acid solution for 1 minute, followed by another rinse in distilled water. Sections then underwent dehydration and mounting as described above.

Masson's Trichrome stains collagen blue. To analyze this staining, images were taken using an LMI-3000 Series Routine Inverted Microscope (Laxco, WA, USA) at 10X magnification with a SeBaCam Digital Camera (PN: SeBaCam100; Laxco, WA, USA) and SeBaView software (Laxco, WA, USA) (Fig. 10). Using ImageJ (National Institutes of Health, MA, USA), the colour threshold was adjusted (threshold method: default ; threshold colour: black ; colour space: RGB). Colour settings for red, green, and blue were all set to 0 for low and 255 for high. The green colour threshold was slowly decreased until the tissue area appeared black. The area of slide occupied by tissue was measured. Colour thresholds were reset back to 0 for low and 255 for high. The red colour threshold was then

lowered until only the area that stained blue appeared black. This resulted in some non-specific selection of tissue. To ensure that only areas stained blue were selected, the blue colour threshold was adjusted to increase specificity. The blue stained was then measured. Presence of collagen was calculated to be percent of blue tissue stained ([area of blue stained tissue / total area of tissue] *100%). This analysis was conducted blinded. Presence of collagen was compared between all three groups.

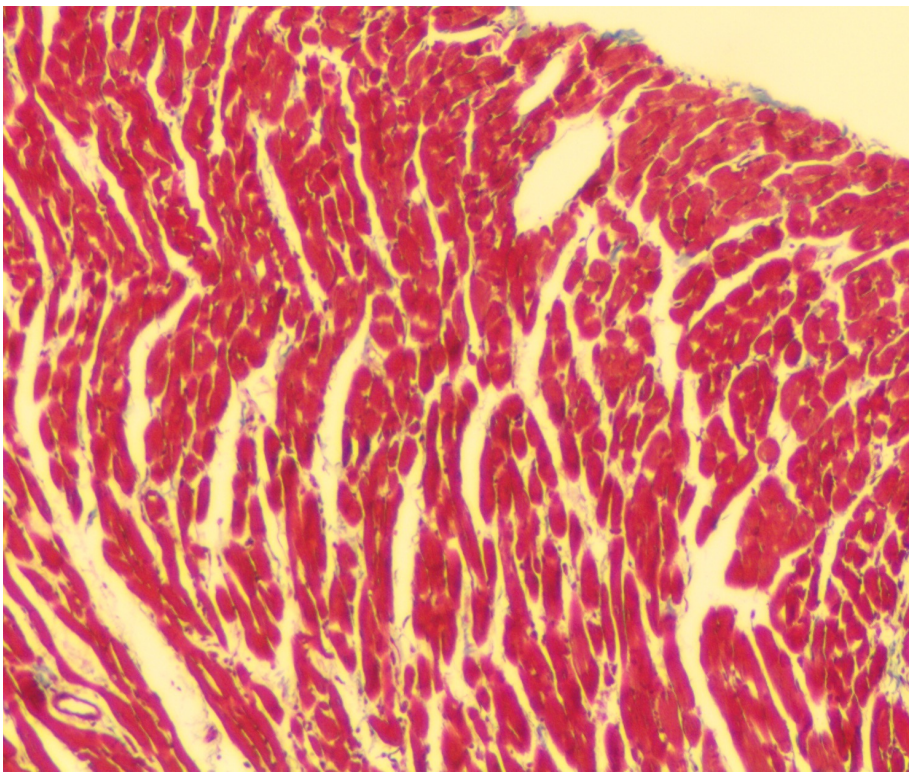

Figure 10. Representative image of Masson's Trichrome staining for fibrosis.

3.15 Statistical Analyses

Values are presented as mean ± standard deviation (St.Dev). Comparison of values within groups (Baseline vs Pacing) was analyzed by non-parametric paired two-tailed T-test. Comparison of values between groups (Control vs MCT-4 vs. MCT-5) was analyzed by one-way ANOVA with Tukey *post-hoc* tests. Significance for all tests was held at $p < 0.05$. Statistical analysis was performed using Prism 9 (GraphPad Inc, USA).

CHAPTER 4: RESULTS

4.1 Fischer CDF Rats develop progressive PAH in response to MCT injection

4.1.1 Hemodynamic changes in Fischer CDF rat MCT model

MCT rat model is a common model to study PAH and related cardiac remodeling; however, majority of the studies utilize SD rats. We planned to study the Fischer CDF rats due to higher susceptibility of these rats to RV remodeling. First, Fischer CDF rats were treated with MCT (60 mg/kg) and progression of PAH was assessed at 4 and 5 weeks post MCT injection (MCT-4 and MCT-5, respectively). Compared to the naïve (control) group, both MCT-4 and MCT-5 groups showed significant increase in RVSP (Fig. 11A). MCT-5 showed a marked increase in RVSP compared to MCT-4, highlighting progressive PAH in this model (A). Note that some animals included in this study do not have RVSP recorded due to challenges associated with catheterization of the jugular vein (cntrl n=5; MCT-4 n=7; MCT-5 n=4). Furthermore, we assessed PAT:PET ratio and PVR as markers for severity of PAH. PVR increased in MCT-4 and MCT-5 compared to control (C). Consistent with RVSP and PVR, MCT-4 and MCT-5 groups treated with MCT showed decreased PAT:PET compared to controls, showing that the time to peak ejection was shortened as PAH developed and progressed (B).

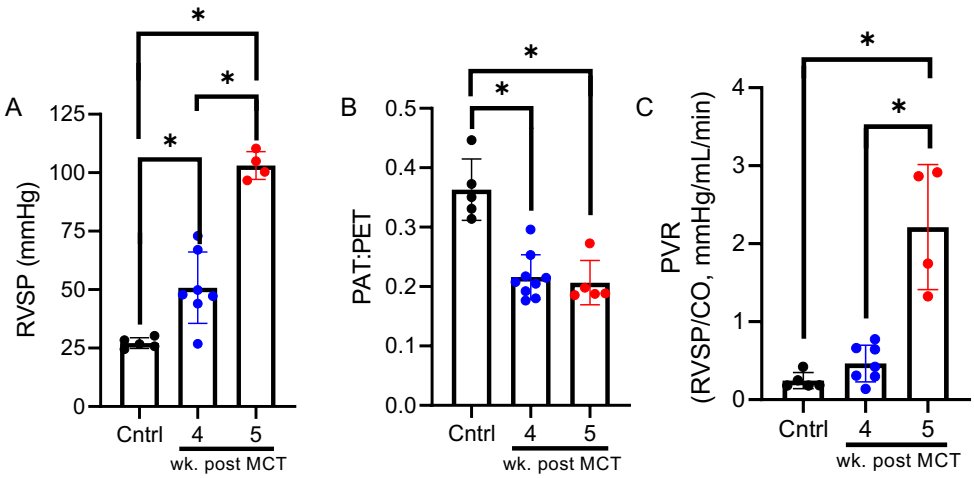

Figure 11. Fischer CDF rats develop progressive PAH following MCT injection. Bar graphs demonstrating (A) RVSP, (B) Pulmonary artery acceleration time to pulmonary ejection time ratio (PAT:PET), and (C) PVR (RVSP/CO) of control, MCT-4 and MCT-5 groups. N= 4-7 per group. Bar graphs represent mean and error bars show standard deviation. Ordinary one-way ANOVA followed by Tukey's multiple comparisons test was used for statistical comparison. *p<0.05.

Table 2. Raw data values of animal statistics throughout MCT model.

Group	Age (weeks)	BW Day 0 (g)	BW Max (g)	BW Study End (g)	Δ BW from Day 0 (g)	Δ from Max BW
CNTRL	**10**	212.0	N/A	N/A	N/A	N/A
CNTRL	**10**	210.6	N/A	N/A	N/A	N/A
CNTRL	**10**	218.3	N/A	N/A	N/A	N/A
CNTRL	**10**	229.6	N/A	N/A	N/A	N/A
CNTRL	**10**	215.8	N/A	N/A	N/A	N/A
Mean	**10**	**218.6**				
MCT-4	13	243.5	266.7	266.7	23.2	0.0
MCT-4	13	244.1	270.2	250.7	6.6	-19.5
MCT-4	13	227.7	251.5	220.0	-7.7	-31.5
MCT-4	14	206.3	233.3	207.3	1.0	-26.0
MCT-4	14	211.3	242.5	222.4	11.1	-20.1
MCT-4	14	233.6	260.1	254.3	20.7	-5.8
MCT-4	14	216.0	237.7	202.9	-13.1	-34.8
MCT-4	14	242.0	255.7	247.8	5.8	-7.9
MCT-4	14	223.0	240.8	232.0	9.0	-8.8
Mean	**13.67**	**227.50**	**250.94**	**233.79**	**6.29**	**-17.16**
MCT-5	15	210.0	222.4	183.4	-26.6	12.40
MCT-5	15	190.0	215.6	183.9	-6.1	25.60
MCT-5	15	173.8	216.4	187.4	13.6	42.60
MCT-5	15	197.6	241.6	214.5	16.9	44.00
MCT-5	15	188.1	210.6	181.6	-6.5	22.50
Mean	**15**	**191.9**	**221.32**	**190.16**	**-1.74**	**29.42**

4.1.2 Progressive changes in RV structure in Fischer CDF rat MCT model

Consistent with hemodynamic changes, both MCT-4 and MCT-5 groups showed increase in Fulton index compared to control group (0.35 ± 0.06, 0.47 ± 0.05 and 0.25 ± 0.05, respectively) (Fig. 12A). H&E staining confirmed the hypertrophy on a cellular level (B). Compared to control group, MCT-4 and MCT-5 showed a significant increase in myocyte cross-sectional area (C). Histological analyses were conducted blinded. Furthermore, echocardiographic assessment showed increased RV anterior wall thickness (RVAW) of MCT-5 rats during both systole and diastole compared to controls (Fig.13a&C). RVAW of rats in the MCT-4 group was significantly higher than control during systole (B). Furthermore, enlargement of RV chamber was observed in MCT-5 groups as the ratio of RVIDd/LVIDd significantly increased in MCT-5 when compared to both control and MCT-4 (D), demonstrating severe RV dilation in the MCT-5 group. Echocardiographic analysis was not conducted blinded.

Table 3. Raw data collected from echocardiographic assessment and whole-heart separation.

Group	Δ from Max BW	RV Mass (g)	LV+S Mass (g)	RVAs	RVAd	RVAWd	RVAWs	Fractional Area Change	Fractional Shortening
CNTRL	N/A	0.18	0.58	26.54	40.25	0.91	1.26	0.34	0.28
CNTRL	N/A	0.18	0.64	26.17	40.68	0.89	1.49	0.36	0.40
CNTRL	N/A	0.16	0.69	20.05	29.38	0.76	1.12	0.32	0.32
CNTRL	N/A	0.12	0.60	23.23	30.58	0.81	1.09	0.24	0.26
CNTRL	N/A	0.14	0.63	9.38	16.72	0.88	1.51	0.44	0.42
Mean		**0.16**	**0.63**	**21.07**	**31.52**	**0.85**	**1.29**	**0.34**	**0.34**
MCT-4	23.2	0.16	0.66	28.53	47.98	1.44	2.55	0.41	0.44
MCT-4	26.1	0.19	0.65	25.04	35.08	1.11	2.13	0.29	0.48
MCT-4	23.8	0.21	0.57	23.90	35.72	1.54	2.50	0.33	0.38
MCT-4	27.0	0.23	0.59	27.90	41.00	1.61	2.53	0.32	0.41
MCT-4	31.2	0.20	0.54	28.97	40.14	1.62	2.76	0.28	0.47
MCT-4	26.5	0.22	0.70	26.90	41.06	1.36	2.56	0.34	0.36
MCT-4	21.7	0.19	0.60	30.54	41.31	1.40	2.19	0.26	0.37
MCT-4	13.7	0.20	0.58	23.96	37.69	1.85	2.97	0.36	0.50
MCT-4	17.8	0.32	0.68	24.84	38.24	1.00	2.01	0.35	0.33
Mean	**23.44**	**0.21**	**0.62**	**26.73**	**39.80**	**1.44**	**2.47**	**0.33**	**0.42**
MCT-5	12.40	0.19	0.56	47.18	54.06	2.77	3.56	0.13	0.22
MCT-5	25.60	0.34	0.64	50.75	61.20	3.12	4.28	0.17	0.27
MCT-5	42.60	0.32	0.70	61.44	72.29	3.50	5.17	0.15	0.27
MCT-5	44.00	0.34	0.69	34.10	46.36	2.77	3.75	0.26	0.26
MCT-5	22.50	0.28	0.70	35.94	46.27	2.48	3.88	0.22	0.36
Mean	**29.42**	**0.29**	**0.66**	**45.88**	**56.04**	**2.93**	**4.13**	**0.19**	**0.28**

Group	RVIDd (mm)	LVIDd (mm)	RVIDd/LVIDd	HR (Echo, bpm)	Stroke Volume (mL)	Cardiac Output (mL/min)
CNTRL	1.23	6.30	0.19	371.62	0.29	107.14
CNTRL	0.90	6.76	0.13	381.63	0.44	167.87
CNTRL	0.64	3.03	0.21	277.78	0.24	67.09
CNTRL	0.82	2.71	0.30	338.03	0.41	138.64
CNTRL	0.81	1.97	0.41	403.36	0.33	134.52
Mean	**0.88**	**4.15**	**0.25**	**354.48**	**0.34**	**123.05**
MCT-4	3.64	5.96	0.61	343.68	0.57	195.02
MCT-4	2.63	4.97	0.53	322.87	0.20	64.15
MCT-4	2.80	4.41	0.64	451.23	0.21	93.91
MCT-4	3.50	4.99	0.70	329.14	0.21	70.22
MCT-4	2.23	5.08	0.43	326.68	0.31	101.25
MCT-4	3.13	4.07	0.77	417.11	0.25	103.89
MCT-4	3.81	4.59	0.83	381.71	0.30	113.46
MCT-4	2.43	4.08	0.59	381.19	0.37	142.93
MCT-4	1.97	3.48	0.57	357.62	0.44	158.51
Mean	**2.90**	**4.63**	**0.63**	**367.91**	**0.32**	**115.93**
MCT-5	3.17	2.12	1.49	366.97	0.21	75.68
MCT-5	4.78	2.09	2.29	314.02	0.11	33.17
MCT-5	2.33	2.30	1.01	387.93	0.11	42.15
MCT-5	3.18	2.14	1.49	358.21	0.17	60.09
MCT-5	2.10	2.40	0.88	295.83	0.13	38.52
Mean	**3.11**	**2.21**	**1.43**	**344.59**	**0.14**	**49.92**

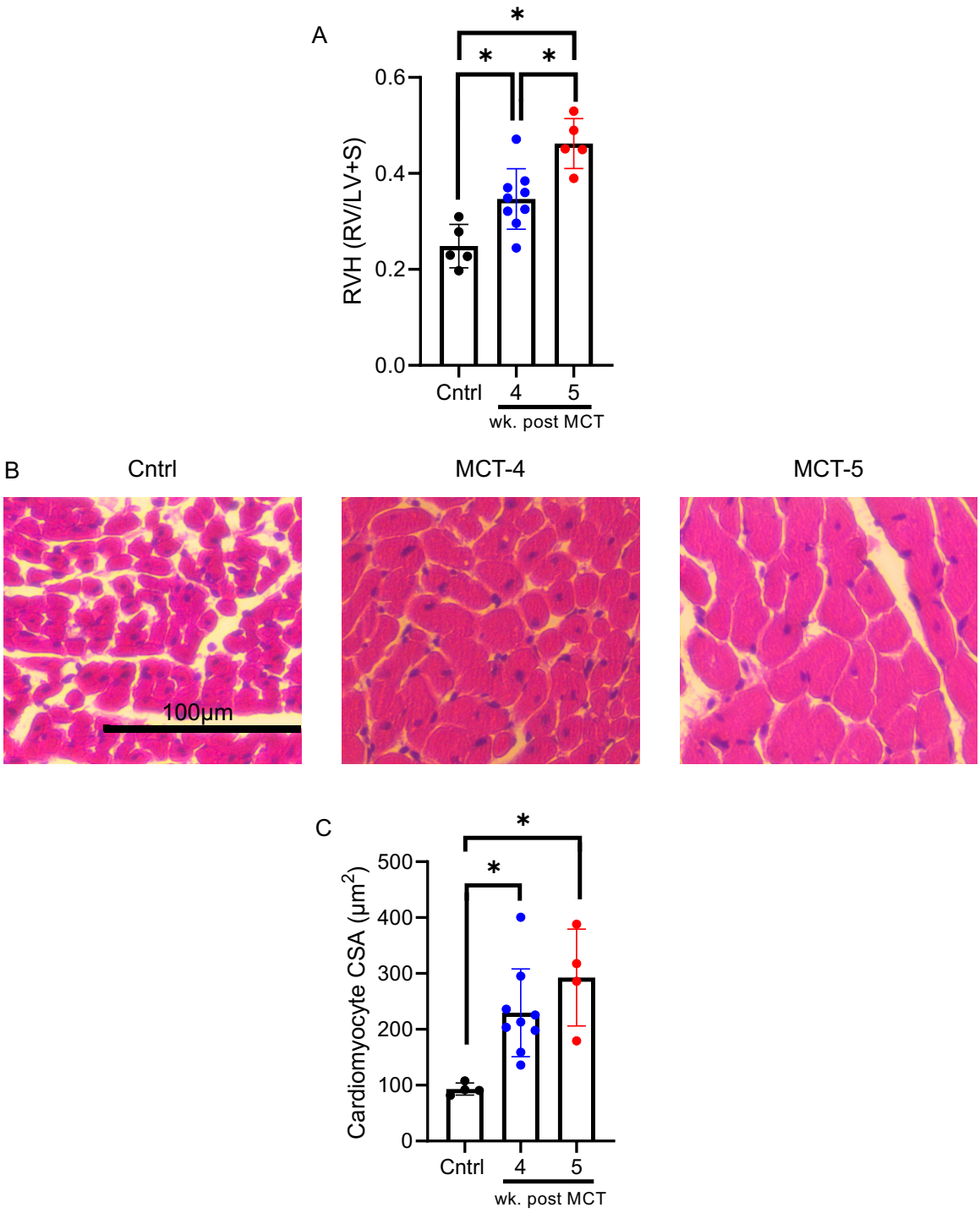

Figure 12. PAH in Fischer CDF rat MCT model leads to RV hypertrophy. (A) Bar graph representing RV Hypertrophy. (B) Representative images, taken at 20X, of hematoxylin and eosin staining of RV sections from control, MCT-4, and MCT-5 groups. (C) Bar graph showing mean cross-sectional area of RV cardiomyocytes for control, MCT-4, and MCT-5 groups. Bar graphs represent mean, and error bars show standard deviation. N=4-9 per group, 20 myocyte tracings per animal. Ordinary one-way ANOVA followed by Tukey's multiple comparisons tests were used for statistical comparison. *p<0.05.

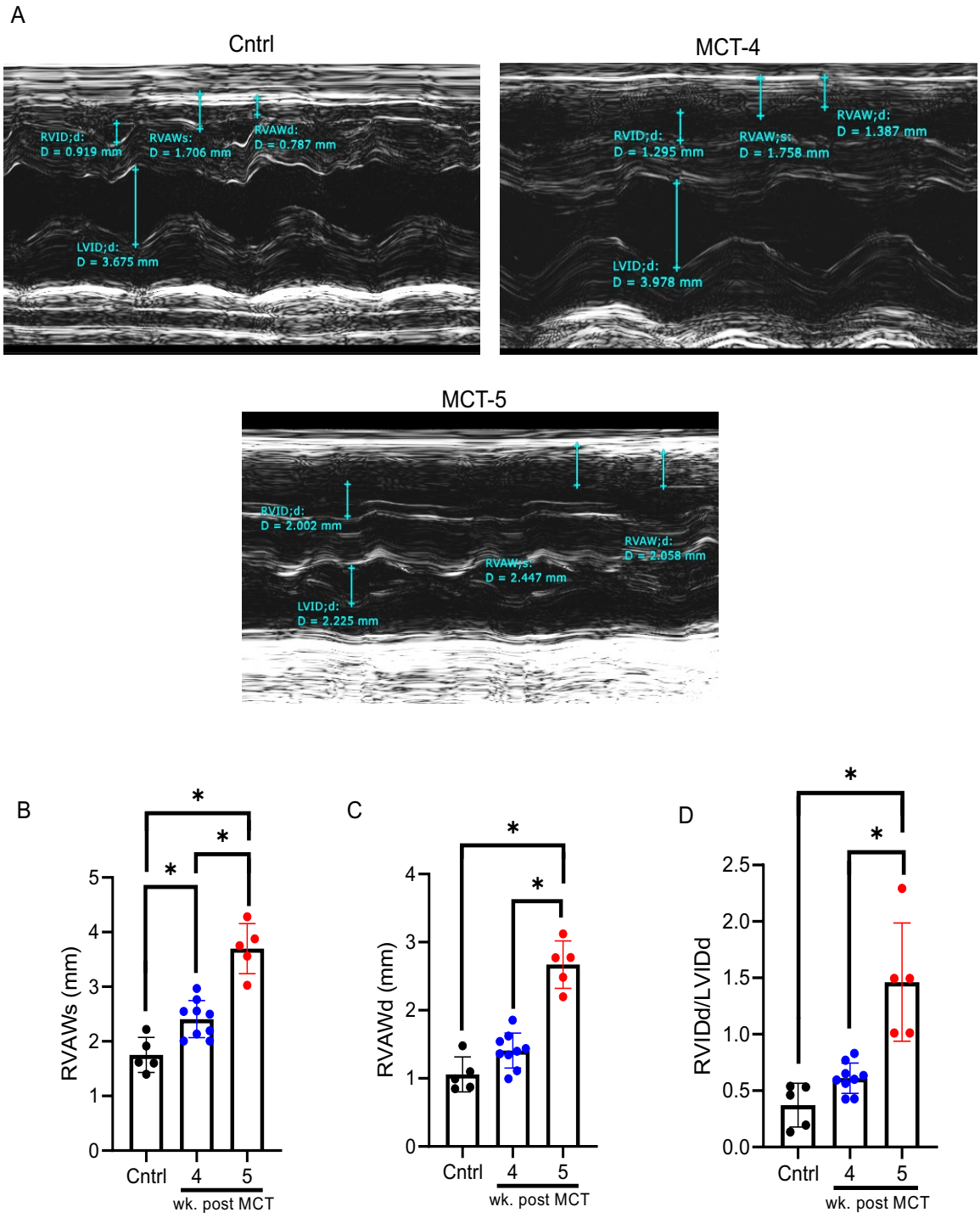

Figure 13. PAH in Fischer CDF rat MCT model leads to progressive RV remodeling. (A) Representative M-mode echocardiography images of control, MCT-4, and MCT-5 groups. Bar graph demonstrating (B) right ventricular anterior wall thickness during systole (RVAWs), (C) right ventricular anterior wall thickness during diastole (RVAWd), and (D) ratio of RV and LV internal diameter during diastole (RVIDd/LVIDd). Bar graphs represent mean, and error bars show standard deviation. N=5-9 per group. Ordinary one-way ANOVA followed by Tukey's multiple comparisons test were used for statistical comparison. *p<0.05.

4.3.3 RV Function in Fischer CDF Rat MCT Model

We assessed changes in RV function using echocardiography (Fig. 14A). Cardiac index (CI), FS, and FAC were calculated as estimated surrogates for cardiac function. CI was significantly decreased in the MCT-5 group compared to both control and MCT-4 (B). Similarly, MCT-5 rats displayed decreased FS and FAC compared to both control and MCT-4 (FS, Control: 0.40 ± 0.05; MCT-4: 0.42 ± 0.06; MCT-5: 0.28 ± 0.05; FAC (%), Control: 33.8 ± 7.1; MCT-4: 31.3 ± 6.6; MCT-5: 18.7 ± 5.9) (C-D). No significant difference was observed between MCT-4 and control groups for CI, FAC or FS.

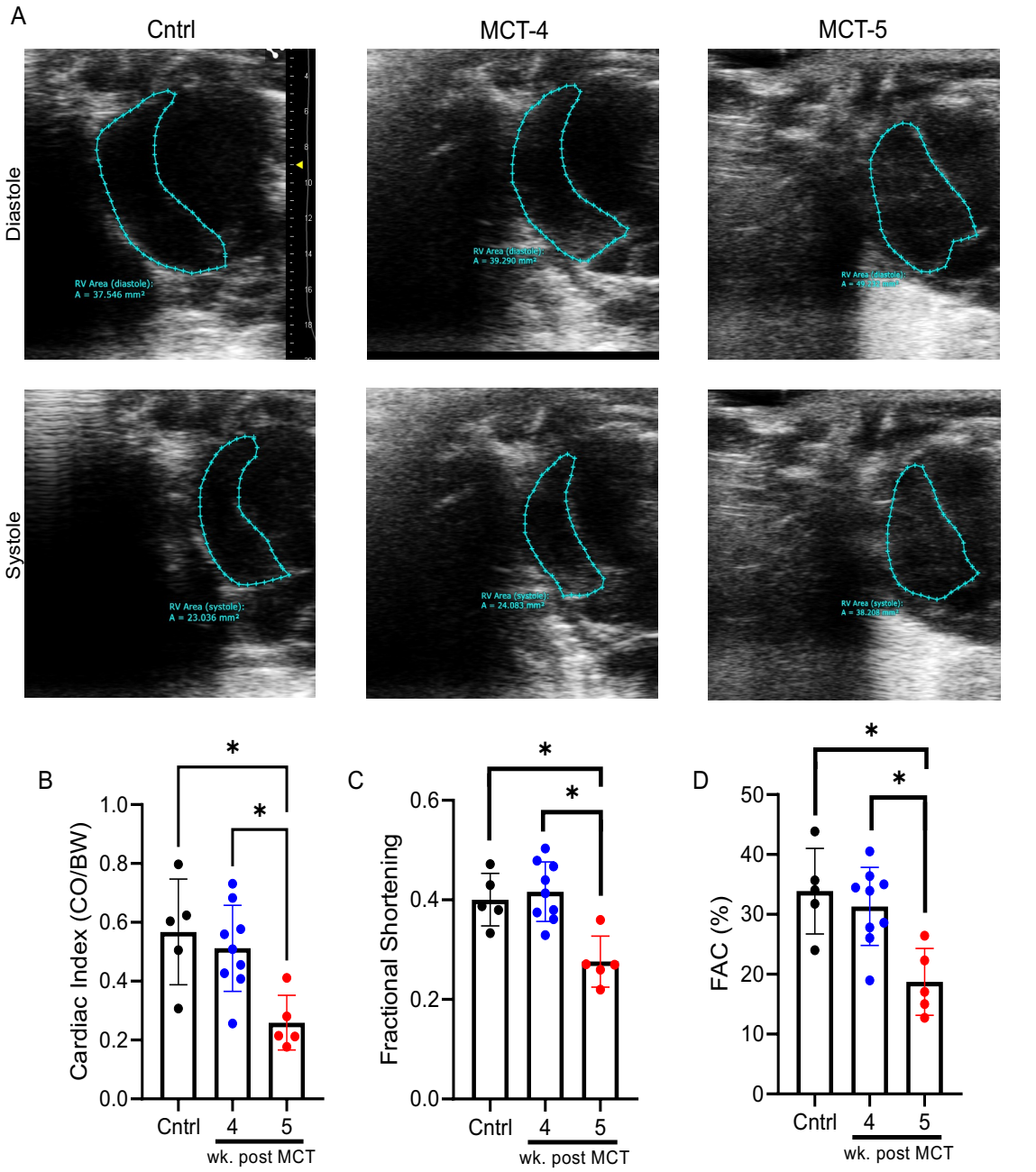

Figure 14. PAH in Fischer CDF MCT rat model leads to decline in cardiac function. (A) B-Mode images of the RV areas of control, MCT-4, and MCT-5 were traced. Top Row represents RV chamber during peak diastole. Bottom row represents RV chamber during peak systole. (B) MCT-5 showed decrease in cardiac index, (C) fractional shortening ((RVIDd–RVIDs)/RVIDd), and (D) fractional area change. Fractional shortening required the assessment of measurements collected in M-Mode, shown in **Figure 13.** Bar graphs represent mean, and error bars show standard deviation. N=5-9 per group. Ordinary one-way ANOVA followed by Tukey's multiple comparisons tests were used for statistical analysis. *p<0.5.

4.2 Fischer CDF Rats undergo electrical remodelling in response to MCT injection

4.2.1 Baseline electrical activity collected from Langendorff-perfused hearts.

The optical mapping / pacing protocol was comprised of multiple rounds of data collection (Fig. 6). After establishing isolated heart perfusion, experimental protocol duration was between 60-90 minutes. To assess the stability of preparation and effect on electrical activity during experimental protocol, we compared the data collected from baseline recordings taken throughout the duration of the optical mapping experiments (Fig. 15). Between both rounds of baseline recordings, there were no changes in HR (A), dF/dt_{max}(B), APD_{20} (C), APD_{50} (D), APD_{80} (E).

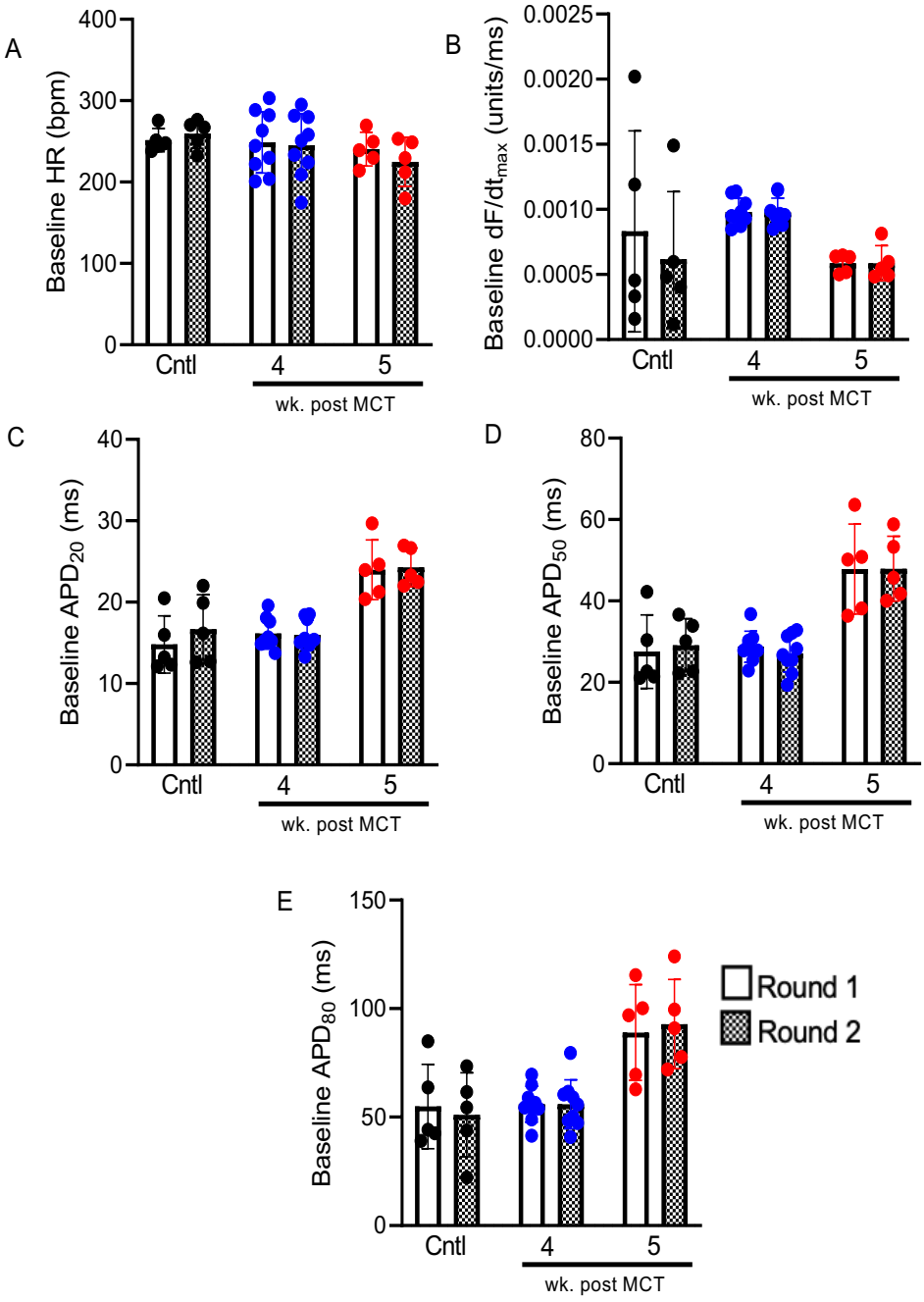

Figure 15. Langendorff-perfused hearts did not change in baseline activity throughout experimental protocol. Measurements of (A) heart rate (HR), (B) dF/dt_{max}, (C) APD_{20}, (D) APD_{50}, and (E) APD_{80} were collected during two separate rounds of recording, per the pacing protocol described. Bar graphs show mean and error bars represent standard deviation. N=5-9 per group. Paired T-test was used for statistical comparison. *p<0.05.

Since there were no changes between rounds of baseline recordings for all three groups, measurements were averaged to make group comparisons (Fig. 16). There were no significant differences in both HR (A) and dF/dt_{max} (B) between control, MCT-4, and MCT-5 groups. There was significant increase in APD_{20}, APD_{50}, and APD_{80} in the MCT-5 group compared to the controls (C-E). However, there was no difference between control and MCT-4 groups for APD_{20}, APD_{50}, and APD_{80}. The APD lengthening was clear in MCT-5 compared to control in representative tracings (F-G).

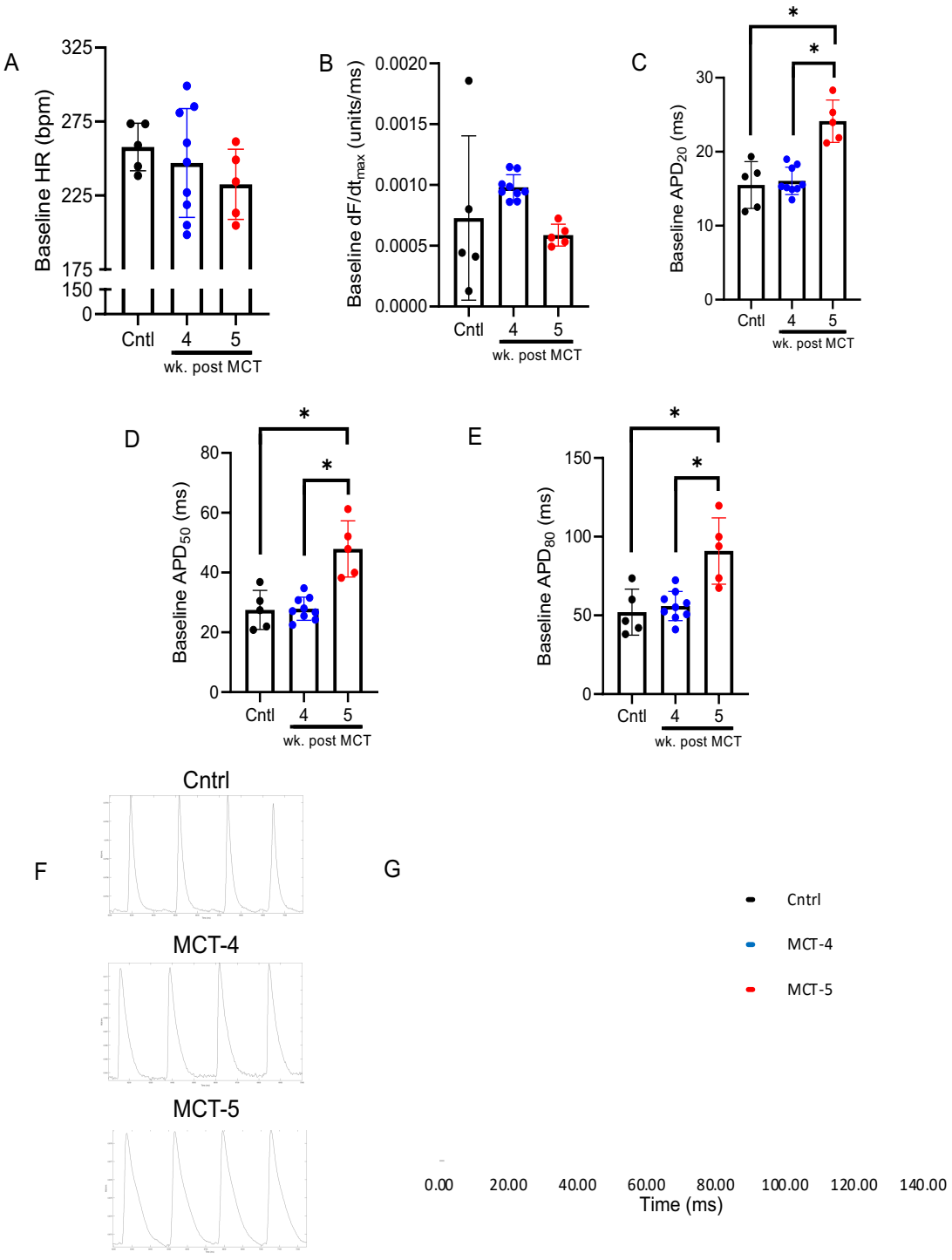

Figure 16. Electrical remodelling was observed in response to severe PAH at baseline. Measurements for (A) heart rate (HR), (B) dF/dt_{max}, (C) APD_{20}, (D) APD_{50}, and (E) APD_{80} from two separate rounds of recording were averaged. (F) A subsection of baseline recordings from control, MCT-4, and MCT-5 groups, followed by (G), the plot of one AP from control, MCT-4, and MCT-5. Bar graphs show mean, and error bars represent standard deviation. N=5-9 per group. Ordinary one-way ANOVA followed by Tukey's multiple comparisons tests were used for statistical comparison. *p<0.05.

4.2.2 Changes to electrical activity following atrial pacing at 5.55 Hz

During the pacing protocol, hearts were paced from the atria at increasing frequencies: 5.55 Hz, 8.33 Hz, and 16.67 Hz. Pacing at any frequency did not trigger arrhythmias. The pacing did not capture 1:1 at frequencies of 8.33 Hz and 16.67 Hz, despite previous studies achieving successful pacing at comparable frequencies [56]. Consequently, the atrial pacing data was analysed for the rounds of pacing at 5.55 Hz. Like the baseline measurements, data from two rounds of atrial pacing have been combined for each group. As expected, heart rate during periods of pacing was similar for all groups (Fig. 17A). There were no significant differences in dF/dt_{max} between groups. APD_{20} and APD_{50} were significantly greater in MCT-5 compared to both MCT-4 and control (B- D). APD_{80} was significantly greater in MCT-5 compared to control (E).

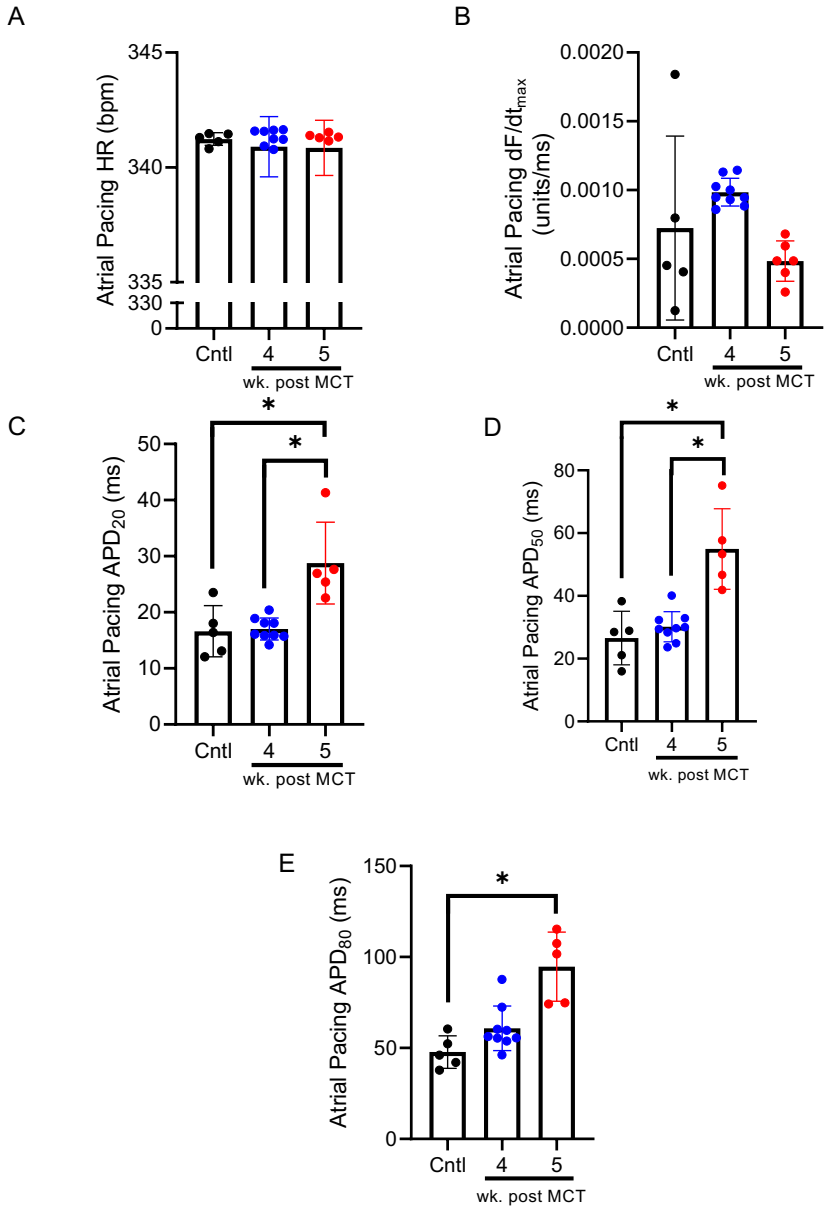

Figure 17. Electrical remodelling was observed in response to severe PAH when paced from the atria at 5.55 Hz. Measurements for (A) heart rate, (B) dF/dt_{max}, (C) APD_{20}, (D) APD_{50}, and (E) APD_{80} from two separate rounds of recording were averaged. Bar graphs show mean, and error bars represent standard deviation. N=5-9 per group. Ordinary one-way ANOVA followed by Tukey's multiple comparisons tests were used for statistical comparison. *$p<0.05$.

4.2.3 Atrial pacing leads to intra-group changes in electrical activity

Significant changes in APD_{20}, APD_{50}, and APD_{80} were seen in response to pacing from the right atria at 5.55 Hz compared to baseline (Fig. 18). As expected, the atrial pacing resulted in a significant increase in HR amongst all groups (A). There were no intra-group differences for dF/dt_{max} (B). Atrial pacing only caused APD_{20} and APD_{80} to increase in MCT-4 (C & E), whilst APD_{50} was increased in all three groups due to atrial pacing (D).

Differences between conditions were then compared against all three groups (Fig. 19). The degree of change with pacing between groups was not statistically significant for HR, APD_{20}, or APD_{80} (A-B & D) between control, MCT-4 and MCT-5 groups. However, the increase in APD_{50} in MCT-5 was significantly greater than the changes in APD_{50} for control and MCT-4 (C).

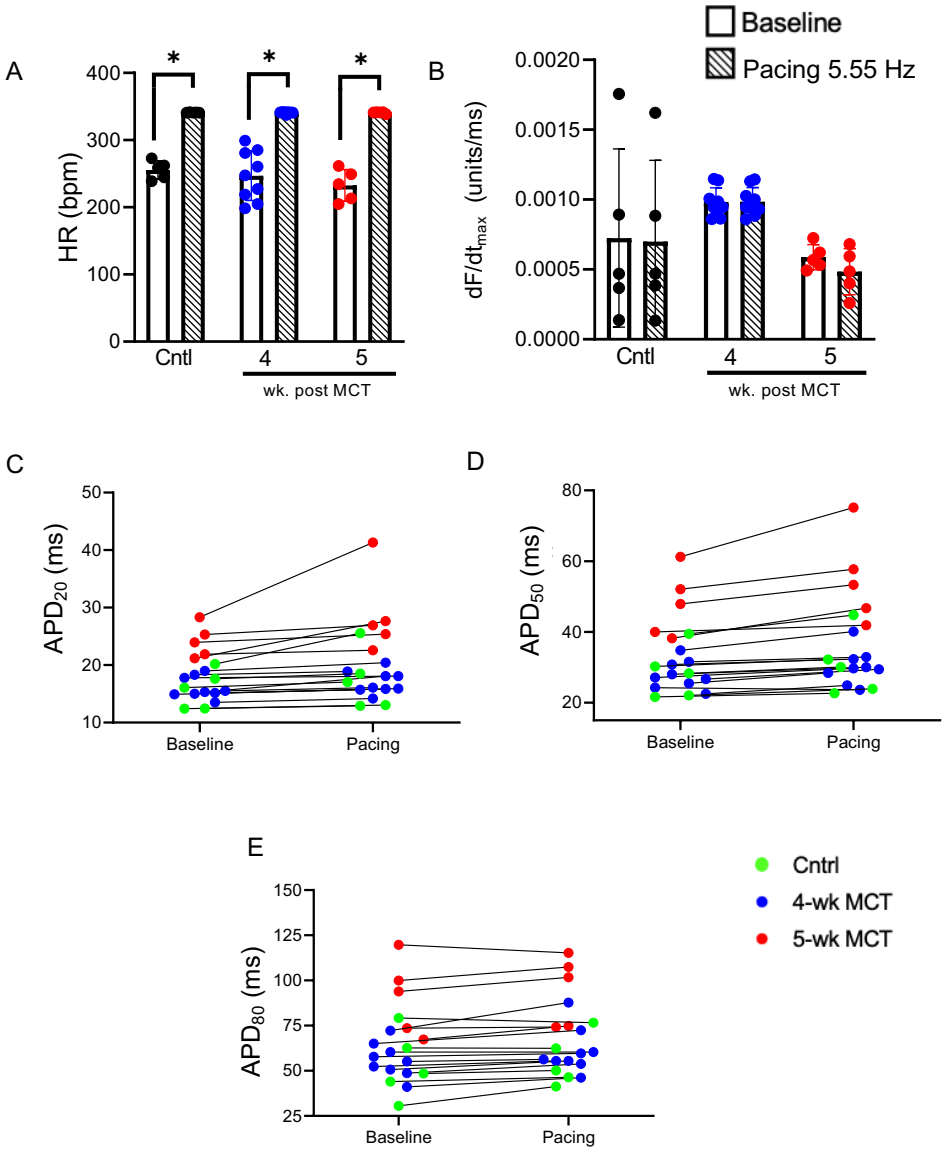

Figure 18. Increased APD was observed in response to severe PAH during atrial pacing compared to baseline activity. Measurements for (A) heart rate, (B) dF/dt_{max}, (C) APD_{20}, (D) APD_{50}, and (E) APD_{80} during baseline and atrial pacing conditions. Bar graphs represent mean, and error bars show standard deviation. N=5-9 per group. Paired T-test was used for statistical comparison. *$p<0.05$.

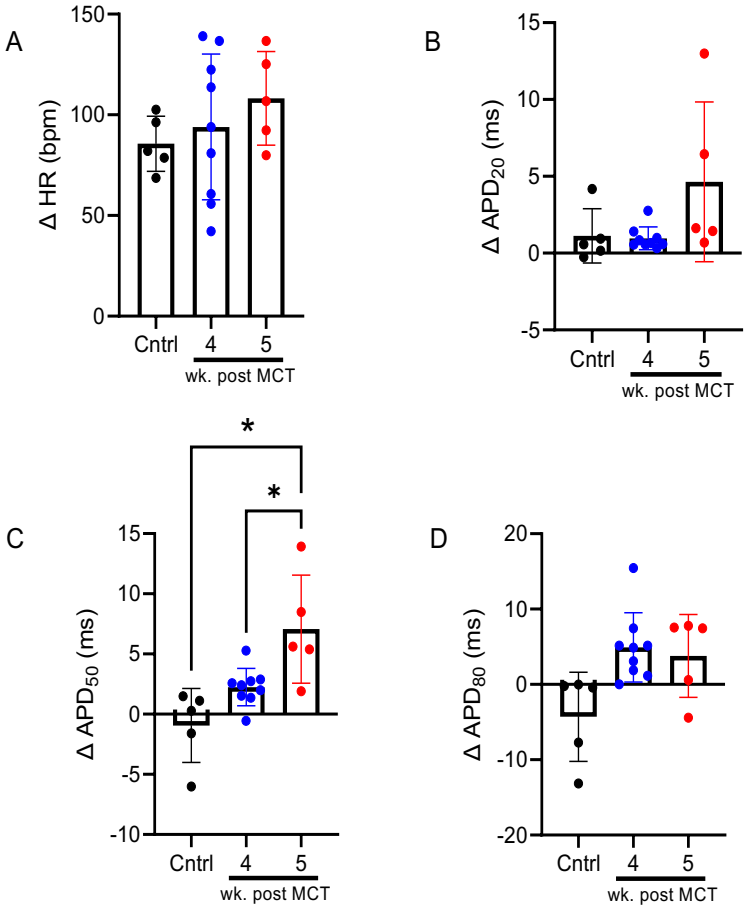

Figure 19. Severe PAH leads to significant lengthening of APD_{50}. Figures comparing differences between atrial pacing and baseline condition for (A) heart rate, (B) APD_{20}, (C) APD_{50}, and (D) APD_{80}. Bar graphs represent mean, and error bars show standard deviation. N=5-9 per group. Ordinary one-way ANOVA followed by Tukey's multiple comparisons tests were used for statistical comparison. *p<0.05.

4.2.4 Ventricular pacing yielded similar observations to atrial pacing in electrical activity.

The pacing protocol also included right ventricular pacing at 5.55 Hz, 8.33 Hz, and 16.67 Hz. Like atrial pacing, no arrhythmias occurred. Pacing at frequencies greater than 5.55 Hz did not consistently capture 1:1; therefore, effects of pacing from ventricle was also only analyzed at pacing frequency 5.5 Hz. Values represent means of two rounds of ventricular pacing. Non-parametric statistical analyses were conducted on this data due to small samples. There were no significant changes in APD_{20}, APD_{50}, and APD_{80} between control and MCT-5 (Fig.20 C-E).

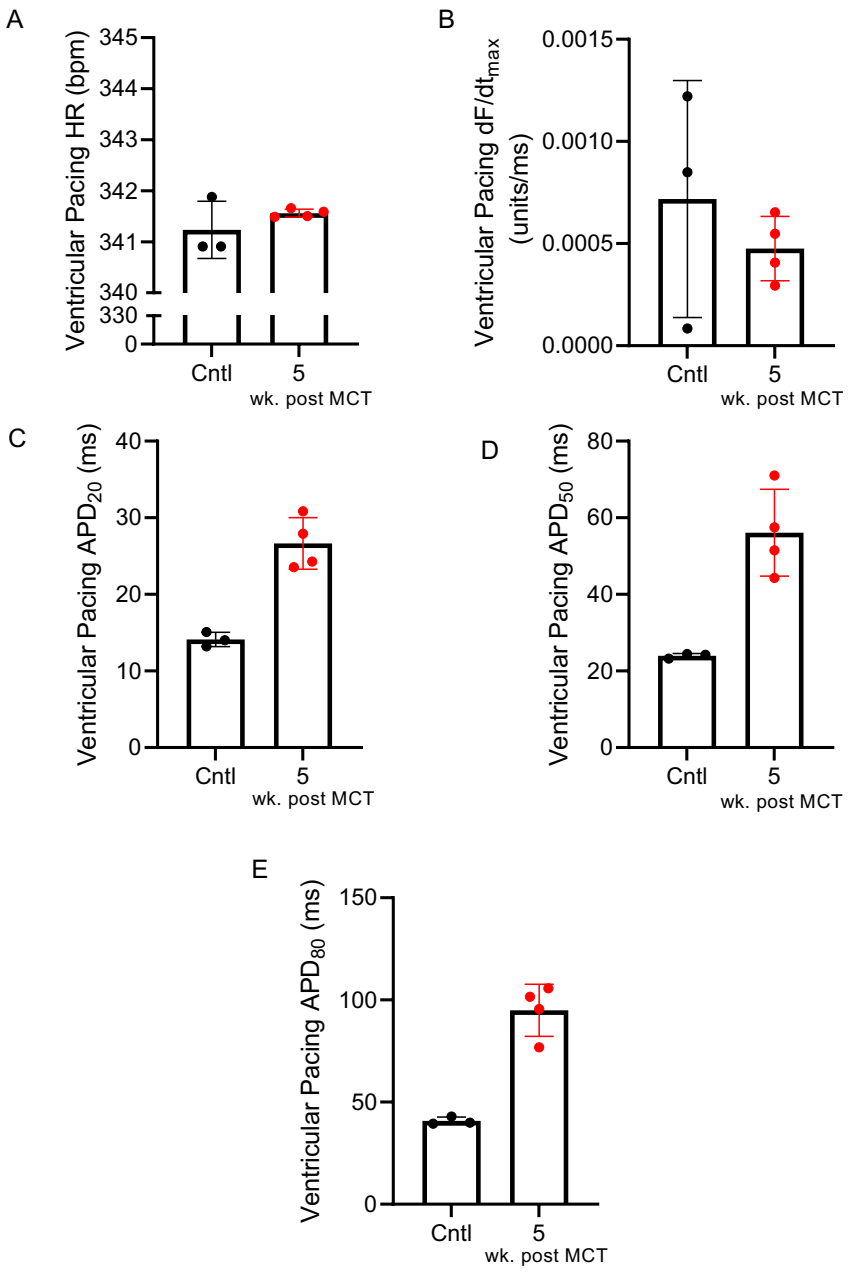

Figure 20. Changes in electrophysiology were observed in response to severe PAH when paced from the ventricle at 5.55 Hz. Measurements for (A) heart rate, (B) dF/dt_{max}, (C) APD_{20}, (D) APD_{50}, and (E) APD_{80} from two separate rounds of recording were averaged. Bar graphs show mean, and error bars represent standard deviation. N=3-7 per group. Non-parametric Unpaired T-test was used for statistical comparison. *$p<0.05$.

4.2.5 Ventricular pacing does not yield the same intra-group differences seen in atrial pacing

Increase in HR was observed in response to ventricular pacing (Fig. 21A). There were no intra-group changes in dF/dt_{max} (Fig 21B). However, contrary to atrial pacing, we did not observe any intra-group differences between baseline activity and ventricular pacing at 5.55 Hz for APD_{20}, APD_{50}, and APD_{80} (Fig 21C-E).

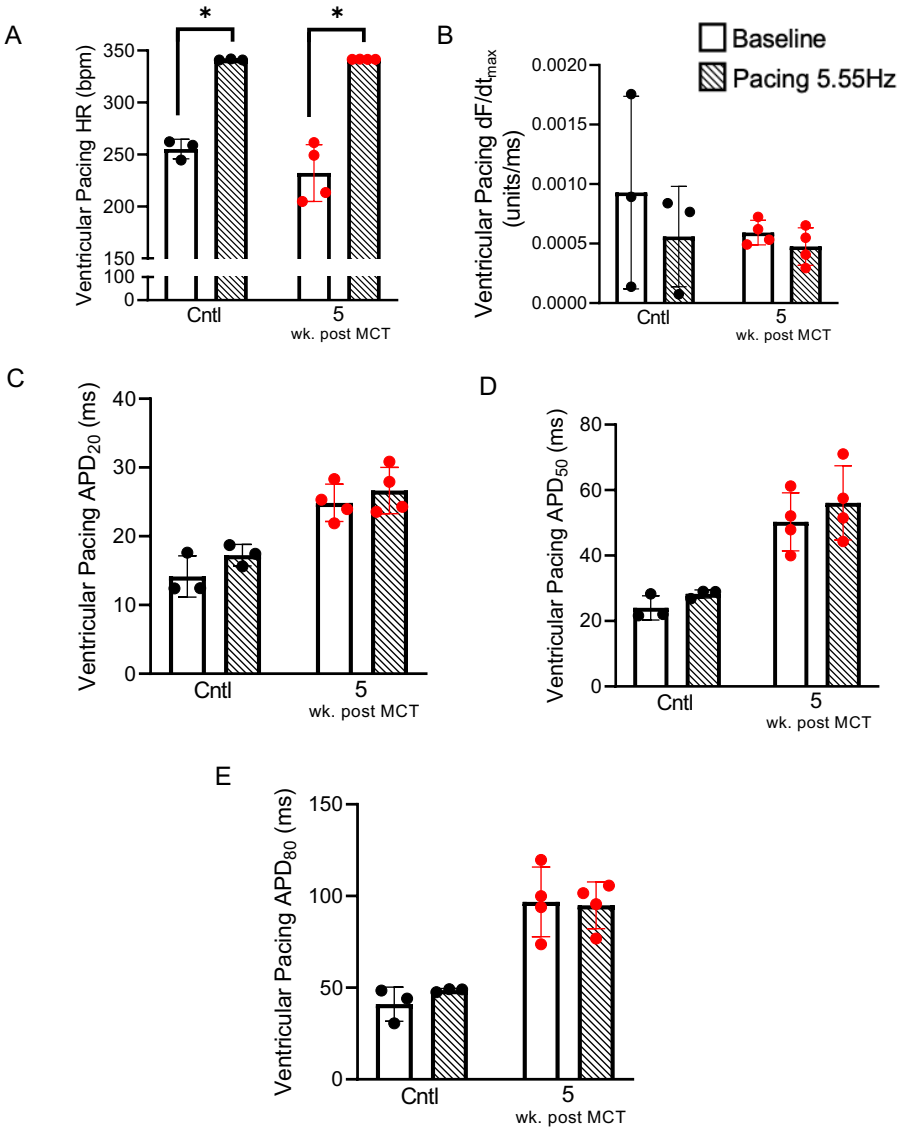

Figure 21. The effects of ventricular pacing were similar to the findings from atrial pacing in MCT-5. Measurements for (A) heart rate (HR), (B) dF/dt_{max}, (C) APD_{20}, (D) APD_{50}, and (E) APD_{80} from two separate rounds of recording were averaged. Bar graphs show mean, and error bars represent standard deviation. N=3-4 per group. Paired T-test was used for statistical comparison. *p<0.05.

4.2.6 Baseline APD_{50} and PAH Disease Severity

The findings related to increased APD_{50} were plotted against both RVSP and RVH, measures used to assess disease severity and progression. When plotted, there is a positive correlation between both APD_{50} and both RVSP (Fig.22 A) and RVH (B).

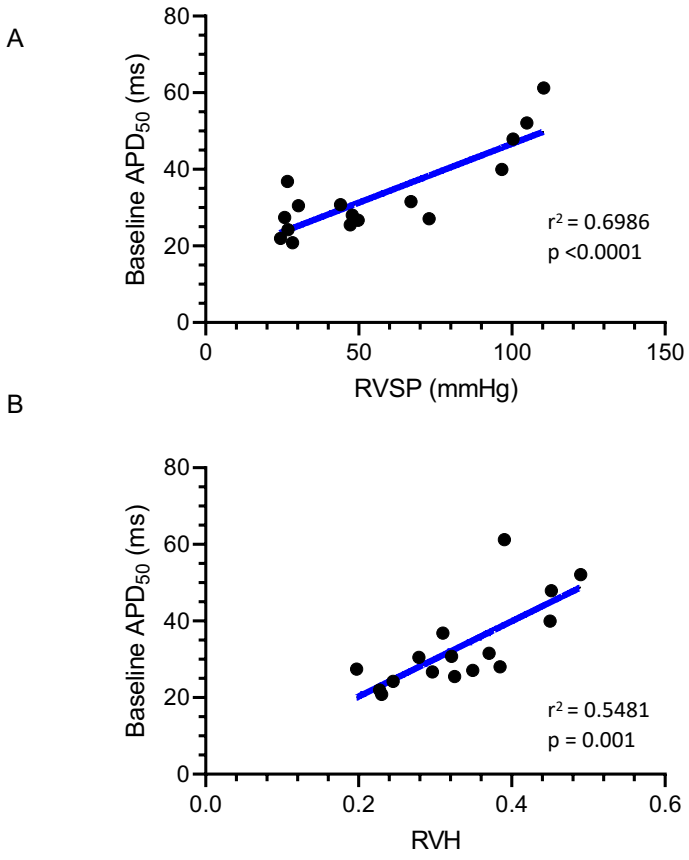

Figure 22. Increased APD_{50} is positively correlated with increased PAH severity. Graph assessing the correlation between APD_{50} and RVSP (A) and RVH (B). N=16. Linear regression analysis was conducted. Correlation coefficient is described on the figures.

4.2.7 Conduction Velocity and APD Heterogeneity

In addition to the measurements described earlier, we were interested in comparing CV and APD heterogeneity (Fig. 23). Conducting ventricular pacing allowed us to measure the CV across the right ventricle. There were no observed differences between control and MCT-5 (A). Surprisingly, under baseline (B) and atrial pacing 5.55 Hz conditions (C), APD heterogeneity was significantly lower in MCT-4. When baseline and atrial pacing 5.55 Hz were compared within groups, we did not observe any intra-group differences (D).

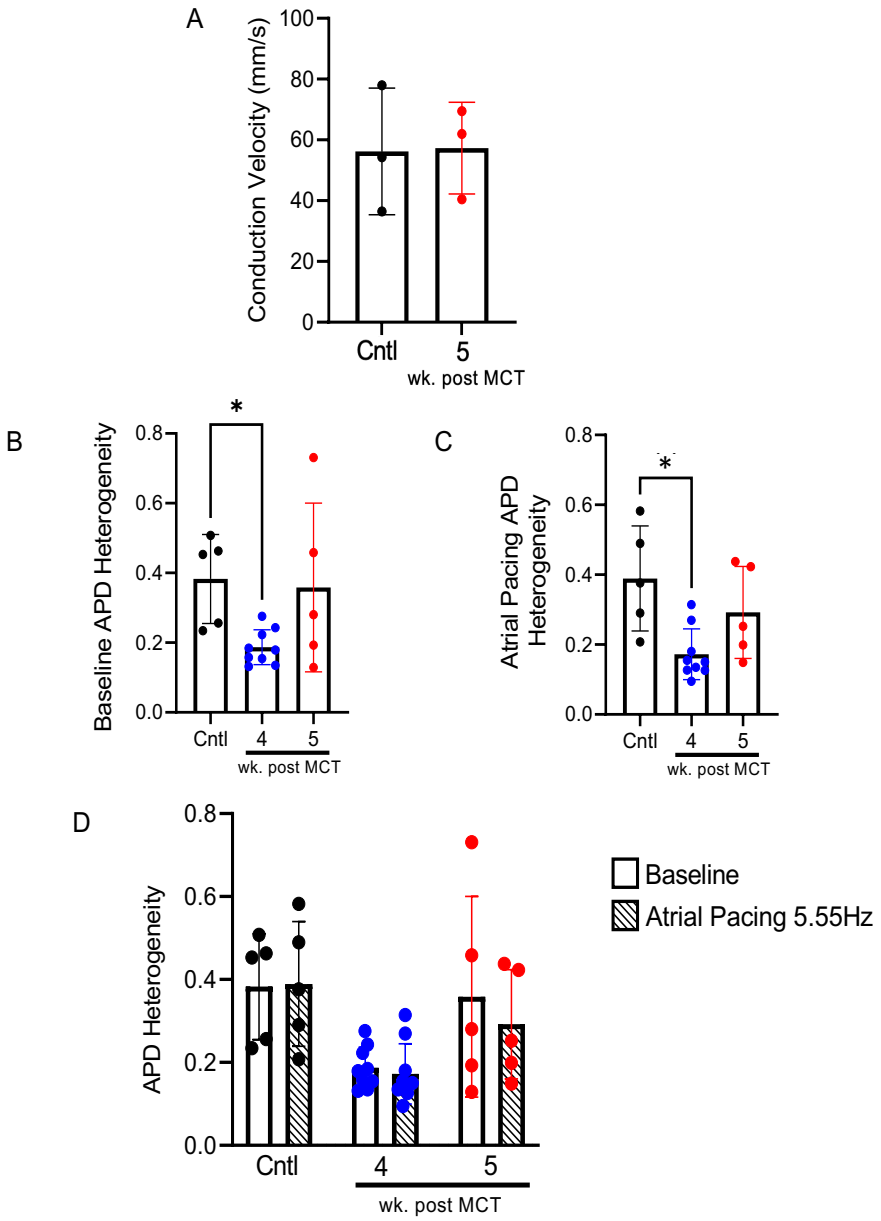

Figure 23. PAH does not result in altered conduction velocity, yet decreased APD heterogeneity was observed in mild PAH. (A) Graph comparing conduction velocity across the right ventricle for control and MCT-5. APD heterogeneity (APD_{80}^{95}- APD_{80}^{5}) / APD_{80}^{50}) was compared between all groups under (B) baseline and (C) ventricular pacing conditions, and (D) then compared within groups. Bars represent mean, and error bars show standard deviation. N=3-9 per group. Ordinary one-way ANOVA was conducted for figures A-C, followed by Tukey's multiple comparisons tests for Figures B and C. Paired T-test was conducted for Figure D. *p<0.05.

4.3 Assessment of RV remodeling as possible contributor to electrical remodeling

4.3.1 Severe PAH in Fischer CDF rat model leads to reduced RV vascular density

Our data showed electrical remodeling of the RV with severe PAH in Fischer CDF rat MCT. Ischemia has been reported as a cause for cardiac arrhythmias, and previous studies have reported reduction in vascular density in the RV during severe PAH that can lead to tissue ischemia [47]. Therefore, first, we assessed vascular density in the RV of control, MCT-4, and MCT-5 rats. Sections of RV were made and stained via IHC for CD31 (Fig. 24A). Vascular density was investigated to screen for any potential signs that ischemia may be present in the MCT-5 groups. Significantly reduced vascular density was seen in the severe PAH group, MCT-5, and a trend towards a decrease in vascular density was observed with MCT-4 (B), compared to the control group.

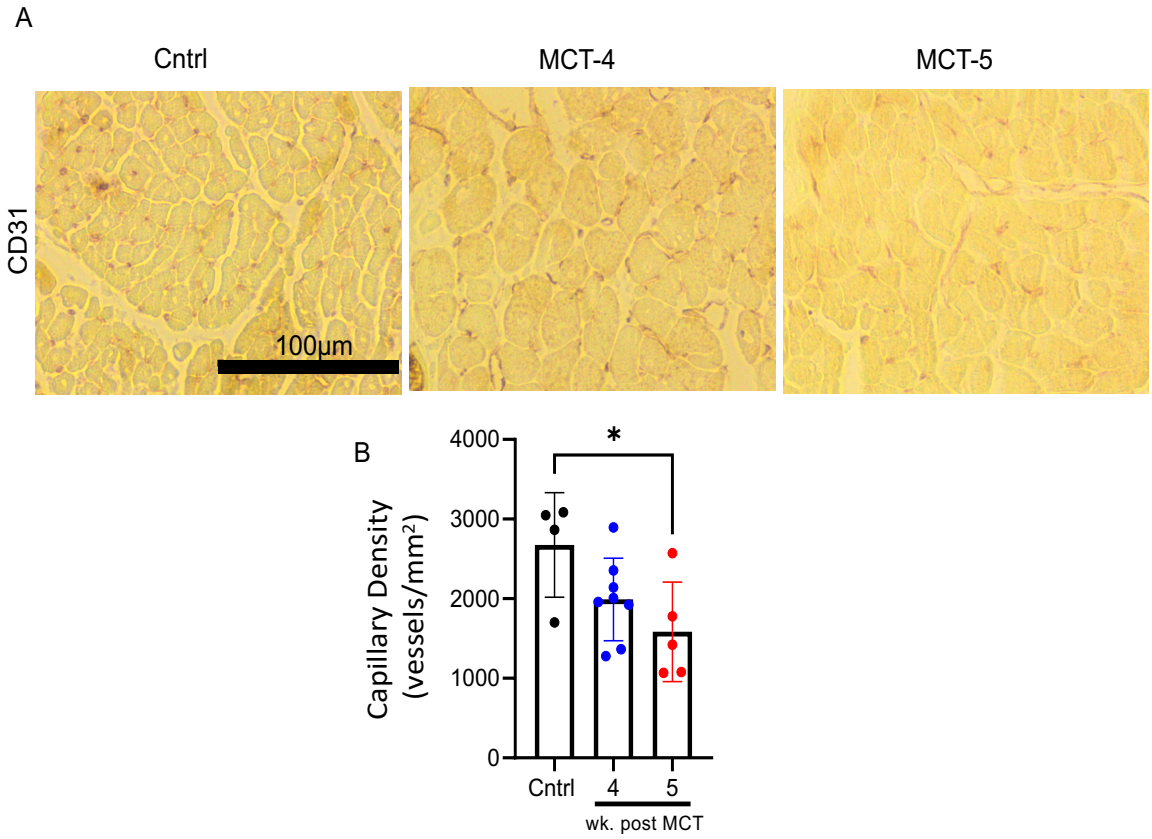

Figure 24. Severe PAH in Fischer CDF rat MCT model leads to decreased vascular density. (A) Representative images, taken at 20X, of immunohistochemistry, performed for CD31 for control, MCT-4, and MCT-5. (B) Bar graph showing mean capillary density (per unit area of the section) for all groups. Bars represent mean, and error bars show standard deviation. N=4-8). Ordinary one-way ANOVA followed by Tukey's multiple comparisons tests were used for statistical comparison. *$p<0.05$.

4.3.2 Fischer CDF rats did not show changes in RV fibrosis in MCT model

Despite RV fibrosis being a hallmark characteristic in many rat models of PAH, we did not observe significant difference between control and MCT-4 or MCT-5 groups (Fig. 25) [14]. Perivascular staining was evident in all groups; however, interstitial collagen staining was not evident in control or MCT-treated groups (A-B).

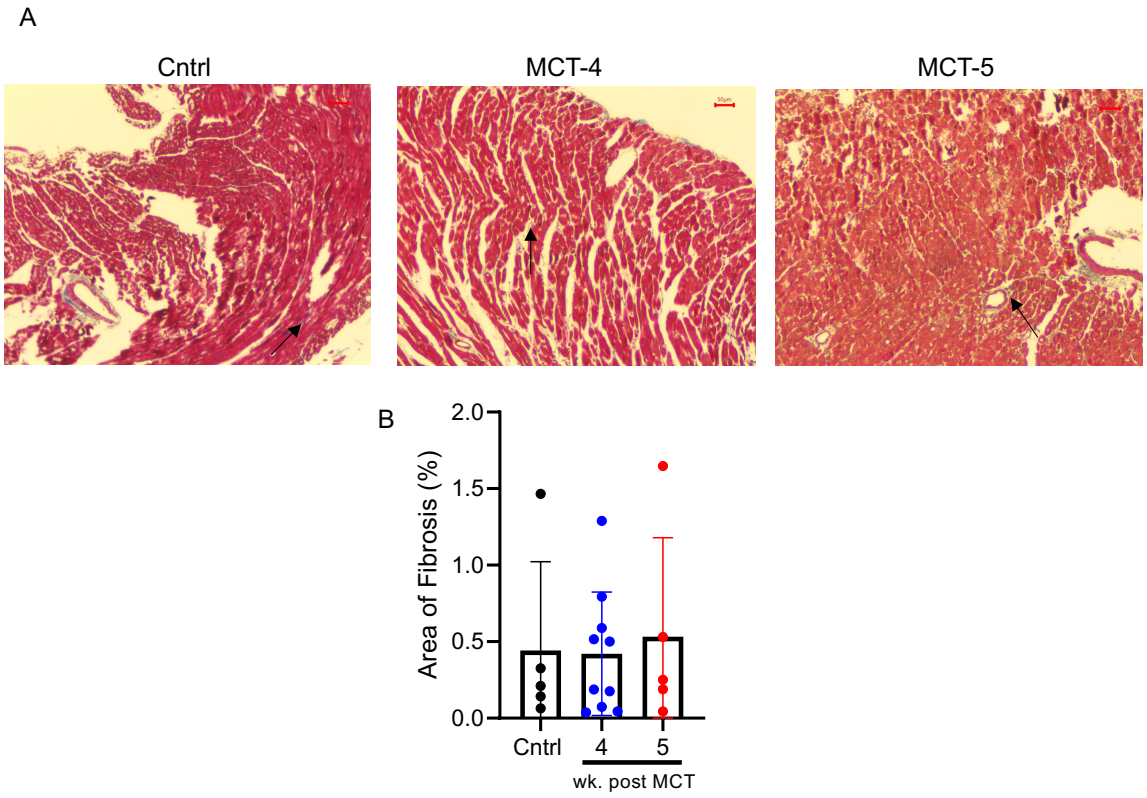

Figure 25. Fischer CDF rat MCT model does not show changes in fibrosis via Masson's Trichrome staining. (A) Representative images, taken at 10X, of Masson's Trichrome staining performed to quantify fibrosis for control, MCT-4, and MCT-5. (B) Graph showing percent area of fibrosis for all groups. Arrows show representative perivascular blue stain (collagen deposition). Bars represent mean, and error bars show standard deviation. N=5-9. Ordinary one-way ANOVA followed by Tukey's multiple comparisons tests were used for statistical comparison. *p<0.05.

4.4 Severe PAH in Fischer CDF rat MCT model did not show abnormalities in electrocardiogram under resting condition.

Prolonged QT intervals have been recorded in human patients with severe PAH [50]. QT duration is inversely related to heart rate. Consequently, we analyzed ECG data from control, MCT-4, and MCT-5 groups (Fig. 26). There were no changes in PR interval (A), RR interval (B), QT interval (C) or QRS interval (E). The QT intervals were also corrected to heart rate (QTc). We found that no difference in QTc amongst all three groups (D) at rest under anesthesia.

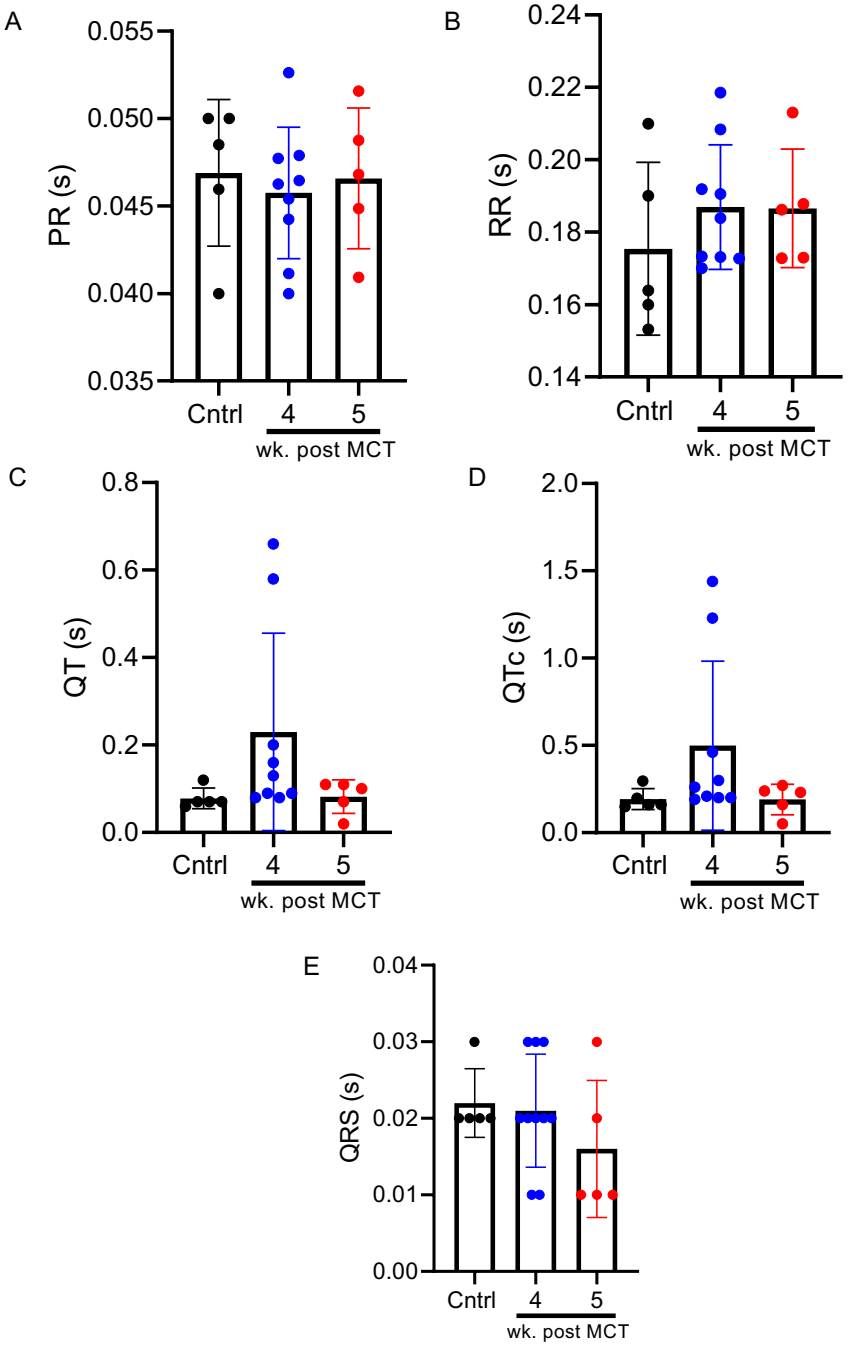

Figure 26. No changes in electrocardiography in response to MCT. PR interval (A), RR interval (B), QT interval (C), QTc (D), and QRS interval. QTc was calculated using the Bazett method. Bar graph represents mean, and error bars show standard deviation. N=5-9 per group.

Table 4. Summary of Observations from the Fischer CDF Rat MCT model of severe PAH. Changes signified with 'X' and '-' signifies no change, compared to baseline.

Observation	MCT-4	MCT-5
Increase in RVSP	X	X
Increase in RVH	X	X
Increase in RVID	-	-
Increase in RVIDd/LVIDd	-	X
Increased RV Wall Thickness	X	X
Decreased Cardiac Index	-	X
Decreased Fractional Area Change	-	X
Decreased Fractional Shortening	-	X
Change in Upstroke Velocity	-	-
Change in Action Potential Duration	-	X
Change in Conduction Velocity	-	-
Change in APD Heterogeneity	X	-
Change in PR Interval	-	-
Change in QTc Interval	-	-
Change in QRS Interval	-	-
Increased Cardiomyocyte CSA	X	X
Decreased Capillary Density	-	X
Increased Fibrosis	-	-

CHAPTER 5: DISCUSSION

5.1 General Discussion

This thesis intended to establish a rat model of severe PAH and utilized optical mapping and other electrophysiological methods for assessment of susceptibility to cardiac arrhythmias in PAH. In response to the MCT injection, Fischer CDF rats developed severe PAH at the 5-week timepoint. At 5 weeks post MCT injection, rats developed severe RV remodeling, showed decline in cardiac function, and were extremely vulnerable to death (more animals reaching humane endpoint). Furthermore, electrical remodeling and reduced vascular density was evident, which may act as a substrate for cardiac arrhythmias and sudden death.

Previously published studies investigating the RV electrophysiology in PAH have reported lengthening of APD. Strauss et al. observed increased APD_{75} in their combinatory model of PAH using Sugen and pneumonectomy in SD rats [51]. The APD_{75} lengthening was also evident during pacing from both the RV and LV [51]. Similarly, Umar et al. found increased APD_{90} in their SD rat MCT model (30-day model, cntrl APD_{90}: 33 ± 6 ms ; MCT APD_{90}: 57 ± 8 ms ($p<0.001$)) [56]. Consistent with the previous reports, the most pronounced finding of this exploratory project was the lengthening of APD in the MCT model in the RHF-susceptible Fischer CDF rats. While previous studies did not explore more than one timepoint, this thesis compared groups at 4 and 5-weeks post MCT injection (MCT-4 and MCT-5, respectively). We observed progressive increase in RVSP and RVH in MCT-4 to MCT-5 groups. While RV function was preserved in MCT-4 group, a decline was observed in MCT-5. Consistent with mal-adaptive remodeling in MCT-5, our study

showed that the observed APD lengthening was only significant in our most severe PAH group, MCT-5. Interestingly, Umar et al. reported 6 spontaneous ventricular fibrillation (VF) initiations in 4 isolated perfused rat hearts of MCT treated SD rats [56]. Contrary to this study, we did not observe spontaneous arrhythmias in our model. Strauss et al., like our study, also did not observe spontaneous VF in their study investigating arrhythmias in Sugen-pneumonectomy model of PAH [51]. Importantly, VF in that study were only observed in response to pacing at a pacing cycle length (PCL) of 60 ms; however, we were only able to reach a PCL of 175 ms. Furthermore, it is understood that APD dispersion heterogeneity is arrhythmogenic [60]. We observed a decrease in APD heterogeneity in MCT-4 compared to control that could be an adaptive response during early mild PAH. However, APD heterogenicity returned to control level indicating loss of adaptive response observed in MCT-4 that, together with increased APD in MCT-5, could contribute to increased arrhythmia susceptibility. In our experiments, we did not observe any incidences of VF/VT, and the underlying mechanisms behind the differences in our study and previously studies are still to be investigated.

RV ischemia is a hallmark feature of severe PAH, where maladaptive remodeling results in non-proportional cardiomyocyte hypertrophy to angiogenesis [15]. In left heart studies, myocardial ischemia has been deemed “inseparable” from mechanisms of electrical remodeling [61]. Lethal arrhythmias are the result of a plethora of pathophysiological abnormalities that interact with coronary vasculature, altered autonomic tone, and metabolic and ionic conditions of the myocardium [61]. Chronic or repeated instances of ischemia produce long-lasting abnormalities to trans-membrane actional potentials and refractory periods [62]. Based on the correlation between ischemia

and sudden cardiac death in left-heart pathologies coupled with the mechanisms of ischemia pertinent to the pathophysiology of PAH, it is likely that RV ischemia is a contributor towards arrhythmias and sudden cardiac death in PAH. Currently, there is a lack of studies investigating the role of RV ischemia in arrhythmias and sudden death in PAH. Our study is the first step towards that and confirmed that there was reduced vascular density in the severe model of PAH. The reduced vascular density may limit blood supply and generate repeated bouts of ischemia during increased cardiac activity in response to physical activity or stress. Overall, results from this thesis form the base for future studies to investigate the link between reduced RV vascular density, RV ischemia, and arrhythmias.

Often, structural heart diseases that favour arrhythmias are accompanied by mechanisms that lead to decreased CV. In humans, PAH results in increased myocardial fibrosis that can lead to decreased conduction velocity and impaired electrical activity [51]. Other mechanisms, like gap junction uncoupling, has also been linked to decreased CV [51]. In the animal study conducted by Strauss et al., increased fibronectin expression was accompanied by increased Col1a1 and Col3a1 expression. This finding was also confirmed by histological staining of RV sections with Sirius Red and Fast Green [51], highlighting increased myocardial fibrosis. When CV was assessed, the group found a moderate decrease at baseline but drastic impairments when paced at increasing rates, ultimately leading to conduction block and induction of ventricular tachycardia (VT) and/or VF [51]. In contrast, our studies show no changes in CV nor fibrosis. This difference could be due to a few different reasons. Firstly, our staining for fibrosis was conducted via Masson's Trichrome; there are alternative staining techniques that could be used to assess fibrosis

such as picrosirius red. Secondly, regarding our assessment of CV, our groups, control and MCT-5, only have a small sample size (n=3 per group). However, our assessment of fibrosis is consistent with previous studies that have shown lower cardiac fibrosis in Fischer CDF rats compared to SD rats [57], [63]. The CV also matches with fibrosis data and suggest that these factors may not be relevant to susceptibility to arrhythmias in this model.

There is some indication that voltage-gated K^+ channel $K_V1.5$ dysfunction plays a mild role in the development of PAH at the level of channel interaction with its subunits [64], [65]. Animal studies investigating K^+ channel activity and expression in PAH have shown decreased transcription and expression of $K_V1.5$ in the RV of SD rats with absolutely no change in transcription or expression in the LV, compared to control [56]. This study also investigated expression of Kv2.1; however, no change in expression of this channel was observed in control vs PAH RVs [56]. As described earlier, Umar et al. observed increased ADP and spontaneous VF that was associated with reduced expression of Kv4.2 and Kv4.3. These studies suggest alteration in K^+ channel in the RV during RV remodeling in response to PAH may play a role in increased APD. The aforementioned K^+ channels are transcribed to I_{KUR}, I_{K1}, and I_{to} [56]. Consistent with previous studies, our results demonstrate increases in APD in severe PAH model; however, we were unable to evaluate expression of ion channels in our study as all the samples were utilized for isolated heart perfusion experiments to assess electrical remodeling. Future investigation should evaluate alteration in expression of various ion channels and assess their role in APD prolongation.

Although similar studies have been conducted investigating electrical remodeling under conditions of PH, specific aspects of those studies differ than ours. The major

difference that separates this thesis from similarly conducted studies is the rat strain; our project utilized the Fischer CDF rat whereas other studies have used the SD rat [51], [56]. As mentioned in the introduction, the Fischer CDF rat has been shown to develop mal-adaptive RV remodeling and show increased mortality and instances of sudden cardiac death [57]. We found it more appropriate to use the rat strain that has a genetic predisposition to increased in a model of PAH. The SD strain has shown to be a model that could be used to study adaptive, compensated RV remodeling. Hence, our study is uniquely designed in the sense that the rat strain chosen for this thesis demonstrates increased mortality and disease severity that is relevant to human disease.

5.2 Limitations

A limitation of this study is the inability to capture pacing at frequencies greater than 5.55 Hz. Despite previous publications (using a different rat strain) presenting data where animals were paced at higher frequencies, we were unable to investigate our model under those conditions. Both atrial and ventricular pacing did not capture 1:1 in our studies. Ultimately, we intended to collect data that would hopefully show increased incidence of arrhythmia or VT/VF. This has been achieved in other studies when paced at frequencies that we were unable to capture. Despite this limitation, changes in electrical activity were still observed in our severe PAH model. Fischer CDF rats have been successfully paced at frequencies higher than we were able to consistently capture, however, the reason behind our inability to do so is still unknown [66]. Further optimization of pacing protocol is needed to address this limitation.

Another limitation of this study is that, due to limitations with time, *in vivo* studies were not conducted. We had intended to study alternative factors that have been established as pro-arrhythmic in left-heart studies such as modulation of ANS and ischemia. *In-vivo* sympathetic activation via Dobutamine administration would have provided insight to cardiac function without having to excise the heart. This set of experiments would have also provided the means to do tissue analysis and genetic expression testing.

Lastly, our controls were age-matched to our MCT groups at the start of the experiment; however, different length of the experiment led to differences in age between all groups at the end study. The control animals were 3-5 weeks younger than the MCT animals at the endstudy, and thus were still in the developmental stage when we conducted. Nonetheless, the bodyweights for the MCT-treated and control rats were similar at the end study; therefore, minimizing the impact of age difference between the groups.

5.3 Future directions

There are many steps that this exploratory project can develop into. Identifying the potential areas of electrical remodeling is only the first step into understanding this facet of PAH. As this project identified electrical changes that are closely related to K^+ channel activity and expression, downstream analyses such as tissue analysis for ion channel transcription, expression, and activity should be considered. Furthermore, isolation of single cardiomyocytes would allow for single-cell techniques such as patch-clamp, to study specific channel activity.

Revisiting mechanisms that lead to arrhythmogenic substrates, introduced in Chapter 1, this study can be progressed and developed to include specific analyses and sub-

analyses that focus on each individual factor. Briefly, *in vivo* animal studies can be conducted to investigate the role of the ANS in electrical remodeling and arrhythmia susceptibility, as hearts that have been excised and perfused via Langendorff apparatus lack central nervous system feedback. *In vivo* studies would also allow for a deeper investigation of the role of ischemia, as there is limited oxygenation capacity, reduced CO, and reduced coronary perfusion in severe PAH [14], [18], [48]. These factors lead to ischemic events that may, in turn, trigger arrhythmias. In our study, all hearts were perfused at the same rate with physiologic buffer. However, *in vivo*, it is possible that the MCT groups were regionally ischemic, and thereby, Langendorff perfusion could have mitigated any possible ischemic trigger. Performing *in vivo* experiments and monitoring animals' electrical activity via ECG could serve as a tool to better understand ANS activity and ischemia as arrhythmogenic substrates in PAH.

Another direction would be to introduce a female control and female MCT group into this study. Research has shown that adult females are more likely to develop PAH than adult males despite females exhibiting less severe disease progression and better survival outcomes [67]. Considering sex as a factor could help uncover some of the mystery behind disease progression and underlying mechanisms.

To uncover any strain or model-specific results, similar studies should be conducted using another model, such has the SUHx model, and another rat strain such as SD. The inclusion of an alternative mode and strain would uncover any variances that have been noted in previous studies as well as allow for a multi-group and multi-model comparative analysis. Female rats have been shown to develop less-severe PAH using the MCT model, and therefore, would not lead to an appropriate comparison between male and female rats.

However, under the SUHx model, both male and female rats have been shown to develop comparable levels of severe PAH and would be a suitable study to compare sexes [67].

5.4 Conclusion

In conclusion, this study has established an easily reproducible rat model of severe PAH as well as techniques and protocols to further study electrophysiology in PAH. We have demonstrated that, in a model of severe PAH, electrical remodeling does. Further research is required to understand the possible underlying mechanism behind each of these factors.

REFERENCES

[1] S. Cassin, *et* al., "THE VASCULAR RESISTANCE OF THE FOETAL AND NEWLY VENTILATED LUNG OF THE LAMB.," *J Physiol*, vol. 171, no. 1, pp. 61–79, May 1964, doi: 10.1113/jphysiol.1964.sp007361.

[2] L. A. Walker and P. M. Buttrick, "The right ventricle: biologic insights and response to disease: updated.," *Curr Cardiol Rev*, vol. 9, no. 1, pp. 73–81, Feb. 2013, doi: 10.2174/157340313805076296.

[3] J. G. E. Zelt, K. R. Chaudhary, V. J. Cadete, L. M. Mielniczuk, and D. J. Stewart, "Medical Therapy for Heart Failure Associated With Pulmonary Hypertension.," *Circ Res*, vol. 124, no. 11, pp. 1551–1567, May 2019, doi: 10.1161/CIRCRESAHA.118.313650.

[4] C. A. Thomas Ryan J Anderson David F Condon Vinicio A de Jesus Perez, "Diagnosis and Management of Pulmonary Hypertension in the Modern Era: Insights from the 6th World Symposium," *Pulm Ther*, vol. 6, doi: 10.6084/m9.figshare.10304645.

[5] S. Hatano, S. Toma, and World Health Organization, "PRIMARY PULMONARY HYPERTENSION Report on a WHO meeting," Geneva.

[6] G. Simonneau *et al.*, "Clinical classification of pulmonary hypertension.," *J Am Coll Cardiol*, vol. 43, no. 12 Suppl S, pp. 5S-12S, Jun. 2004, doi: 10.1016/j.jacc.2004.02.037.

[7] G. Simonneau *et al.*, "Haemodynamic definitions and updated clinical classification of pulmonary hypertension.," *Eur Respir J*, vol. 53, no. 1, Jan. 2019, doi: 10.1183/13993003.01913-2018.

[8] G. Simonneau *et al.*, "Updated clinical classification of pulmonary hypertension.," *J Am Coll Cardiol*, vol. 62, no. 25 Suppl, pp. D34-41, Dec. 2013, doi: 10.1016/j.jacc.2013.10.029.

[9] V. V McLaughlin and M. D. McGoon, "Pulmonary arterial hypertension.," *Circulation*, vol. 114, no. 13, pp. 1417–31, Sep. 2006, doi: 10.1161/CIRCULATIONAHA.104.503540.

[10] H. Gall *et al.*, "The Giessen Pulmonary Hypertension Registry: Survival in pulmonary hypertension subgroups.," *J Heart Lung Transplant*, vol. 36, no. 9, pp. 957–967, Sep. 2017, doi: 10.1016/j.healun.2017.02.016.

[11] S. L. Archer, E. K. Weir, and M. R. Wilkins, “Basic science of pulmonary arterial hypertension for clinicians: new concepts and experimental therapies.,” *Circulation*, vol. 121, no. 18, pp. 2045–66, May 2010, doi: 10.1161/CIRCULATIONAHA.108.847707.

[12] N. W. Morrell *et al.*, “Genetics and genomics of pulmonary arterial hypertension.,” *Eur Respir J*, vol. 53, no. 1, Jan. 2019, doi: 10.1183/13993003.01899-2018.

[13] K. R. Chaudhary, M. Taha, V. J. J. Cadete, R. S. Godoy, and D. J. Stewart, “Proliferative Versus Degenerative Paradigms in Pulmonary Arterial Hypertension: Have We Put the Cart Before the Horse?,” *Circ Res*, vol. 120, no. 8, pp. 1237–1239, Apr. 2017, doi: 10.1161/CIRCRESAHA.116.310097.

[14] J. J. Ryan and S. L. Archer, “The right ventricle in pulmonary arterial hypertension: disorders of metabolism, angiogenesis and adrenergic signaling in right ventricular failure.,” *Circ Res*, vol. 115, no. 1, pp. 176–88, Jun. 2014, doi: 10.1161/CIRCRESAHA.113.301129.

[15] A. L. Frump, S. Bonnet, V. A. de Jesus Perez, and T. Lahm, “Emerging role of angiogenesis in adaptive and maladaptive right ventricular remodeling in pulmonary hypertension.,” *Am J Physiol Lung Cell Mol Physiol*, vol. 314, no. 3, pp. L443–L460, Mar. 2018, doi: 10.1152/ajplung.00374.2017.

[16] S. Heymans *et al.*, “Searching for new mechanisms of myocardial fibrosis with diagnostic and/or therapeutic potential.,” *Eur J Heart Fail*, vol. 17, no. 8, pp. 764–71, Aug. 2015, doi: 10.1002/ejhf.312.

[17] K. Schimmel, K. Ichimura, S. Reddy, F. Haddad, and E. Spiekerkoetter, “Cardiac Fibrosis in the Pressure Overloaded Left and Right Ventricle as a Therapeutic Target.,” *Front Cardiovasc Med*, vol. 9, p. 886553, 2022, doi: 10.3389/fcvm.2022.886553.

[18] C. M. Suen, K. R. Chaudhary, Y. Deng, B. Jiang, and D. J. Stewart, “Fischer rats exhibit maladaptive structural and molecular right ventricular remodelling in severe pulmonary hypertension: a genetically prone model for right heart failure.,” *Cardiovasc Res*, vol. 115, no. 4, pp. 788–799, Mar. 2019, doi: 10.1093/cvr/cvy258.

[19] D. A. Jones, C. W. Benjamin, and D. A. Linseman, “Activation of thromboxane and prostacyclin receptors elicits opposing effects on vascular smooth muscle cell growth and mitogen-activated protein kinase signaling cascades.,” *Mol Pharmacol*, vol. 48, no. 5, pp. 890–6, Nov. 1995.

[20] S. S. Pullamsetti, R. Schermuly, A. Ghofrani, N. Weissmann, F. Grimminger, and W. Seeger, “Novel and emerging therapies for pulmonary hypertension.,” *Am J Respir Crit Care Med*, vol. 189, no. 4, pp. 394–400, Feb. 2014, doi: 10.1164/rccm.201308-1543PP.

[21] O. Sitbon *et al.*, “Selexipag for the Treatment of Pulmonary Arterial Hypertension.,” *N Engl J Med*, vol. 373, no. 26, pp. 2522–33, Dec. 2015, doi: 10.1056/NEJMoa1503184.

[22] A. Giaid and D. Saleh, “Reduced expression of endothelial nitric oxide synthase in the lungs of patients with pulmonary hypertension.,” *N Engl J Med*, vol. 333, no. 4, pp. 214–21, Jul. 1995, doi: 10.1056/NEJM199507273330403.

[23] S. Perrin *et al.*, “New pharmacotherapy options for pulmonary arterial hypertension.,” *Expert Opin Pharmacother*, vol. 16, no. 14, pp. 2113–31, 2015, doi: 10.1517/14656566.2015.1074177.

[24] N. F. Ruopp and B. A. Cockrill, “Diagnosis and Treatment of Pulmonary Arterial Hypertension: A Review.,” *JAMA*, vol. 327, no. 14, pp. 1379–1391, Apr. 2022, doi: 10.1001/jama.2022.4402.

[25] M.-C. Chaumais, E. A. Macari, and O. Sitbon, “Calcium-channel blockers in pulmonary arterial hypertension.,” *Handb Exp Pharmacol*, vol. 218, pp. 161–75, 2013, doi: 10.1007/978-3-642-38664-0_7.

[26] R. M. Tuder *et al.*, “Prostacyclin synthase expression is decreased in lungs from patients with severe pulmonary hypertension.,” *Am J Respir Crit Care Med*, vol. 159, no. 6, pp. 1925–32, Jun. 1999, doi: 10.1164/ajrccm.159.6.9804054.

[27] D. J. Stewart, R. D. Levy, P. Cernacek, and D. Langleben, “Increased plasma endothelin-1 in pulmonary hypertension: marker or mediator of disease?,” *Ann Intern Med*, vol. 114, no. 6, pp. 464–9, Mar. 1991, doi: 10.7326/0003-4819-114-6-464.

[28] N. H. S. Kim and L. J. Rubin, “Endothelin in health and disease: endothelin receptor antagonists in the management of pulmonary artery hypertension.,” *J Cardiovasc Pharmacol Ther*, vol. 7, no. 1, pp. 9–19, Jan. 2002, doi: 10.1177/107424840200700i102.

[29] C. B. Neylon, P. V Avdonin, R. J. Dilley, M. A. Larsen, V. A. Tkachuk, and A. Bobik, “Different electrical responses to vasoactive agonists in morphologically distinct smooth muscle cell types.,” *Circ Res*, vol. 75, no. 4, pp. 733–41, Oct. 1994, doi: 10.1161/01.res.75.4.733.

[30] M. Clozel, G. A. Gray, V. Breu, B. M. Löffler, and R. Osterwalder, “The endothelin ETB receptor mediates both vasodilation and vasoconstriction in vivo.,” *Biochem Biophys Res Commun*, vol. 186, no. 2, pp. 867–73, Jul. 1992, doi: 10.1016/0006-291x(92)90826-7.

[31] T. Masaki, S. Miwa, T. Sawamura, H. Ninomiya, and Y. Okamoto, “Subcellular mechanisms of endothelin action in vascular system.,” *Eur J Pharmacol*, vol. 375, no. 1–3, pp. 133–8, Jun. 1999, doi: 10.1016/s0014-2999(99)00252-6.

[32] G. Maarman, S. Lecour, G. Butrous, F. Thienemann, and K. Sliwa, “A comprehensive review: the evolution of animal models in pulmonary hypertension research; are we there yet?,” *Pulm Circ*, vol. 3, no. 4, pp. 739–56, Dec. 2013, doi: 10.1086/674770.

[33] J. J. Ryan, G. Marsboom, and S. L. Archer, “Rodent models of group 1 pulmonary hypertension.,” *Handb Exp Pharmacol*, vol. 218, pp. 105–49, 2013, doi: 10.1007/978-3-642-38664-0_5.

[34] J. J. LALICH and L. MERKOW, “Pulmonary arteritis produced in rat by feeding Crotalaria spectabilis.,” *Lab Invest*, vol. 10, pp. 744–50, 1961.

[35] M. Shah, K. Patel, and P. B. Sehgal, “Monocrotaline pyrrole-induced endothelial cell megalocytosis involves a Golgi blockade mechanism.,” *Am J Physiol Cell Physiol*, vol. 288, no. 4, pp. C850-62, Apr. 2005, doi: 10.1152/ajpcell.00327.2004.

[36] J. M. Kay, P. Harris, and D. Heath, “Pulmonary hypertension produced in rats by ingestion of Crotalaria spectabilis seeds.,” *Thorax*, vol. 22, no. 2, pp. 176–9, Mar. 1967, doi: 10.1136/thx.22.2.176.

[37] D. Urboniene, I. Haber, Y.-H. Fang, T. Thenappan, and S. L. Archer, “Validation of high-resolution echocardiography and magnetic resonance imaging vs. high-fidelity catheterization in experimental pulmonary hypertension.,” *Am J Physiol Lung Cell Mol Physiol*, vol. 299, no. 3, pp. L401-12, Sep. 2010, doi: 10.1152/ajplung.00114.2010.

[38] H. P. J. Buermans *et al.*, “Microarray analysis reveals pivotal divergent mRNA expression profiles early in the development of either compensated ventricular hypertrophy or heart failure.,” *Physiol Genomics*, vol. 21, no. 3, pp. 314–23, May 2005, doi: 10.1152/physiolgenomics.00185.2004.

[39] H. C. Rosenberg and M. Rabinovitch, “Endothelial injury and vascular reactivity in monocrotaline pulmonary hypertension.,” *Am J Physiol*, vol. 255, no. 6 Pt 2, pp. H1484-91, Dec. 1988, doi: 10.1152/ajpheart.1988.255.6.H1484.

[40] L. Taraseviciene-Stewart *et al.*, “Inhibition of the VEGF receptor 2 combined with chronic hypoxia causes cell death-dependent pulmonary endothelial cell proliferation and severe pulmonary hypertension.,” *FASEB J*, vol. 15, no. 2, pp. 427–38, Feb. 2001, doi: 10.1096/fj.00-0343com.

[41] J. G. Gomez-Arroyo *et al.*, “Downloaded from journals.physiology.org/journal/ajplung at Dalhousie Univ DAL 11762,” *Am J Physiol Lung Cell Mol Physiol*, vol. 302, pp. 363–369, 2012, doi: 10.1152/ajplung.00212.2011.-Severe.

[42] K. Abe *et al.*, “Formation of plexiform lesions in experimental severe pulmonary arterial hypertension.,” *Circulation*, vol. 121, no. 25, pp. 2747–54, Jun. 2010, doi: 10.1161/CIRCULATIONAHA.109.927681.

[43] A. O’Donnell *et al.*, “A Phase I study of the angiogenesis inhibitor SU5416 (semaxanib) in solid tumours, incorporating dynamic contrast MR pharmacodynamic end points.,” *Br J Cancer*, vol. 93, no. 8, pp. 876–83, Oct. 2005, doi: 10.1038/sj.bjc.6602797.

[44] A. Hyduk, J. B. Croft, C. Ayala, K. Zheng, Z.-J. Zheng, and G. A. Mensah, “Pulmonary hypertension surveillance--United States, 1980-2002.,” *MMWR Surveill Summ*, vol. 54, no. 5, pp. 1–28, Nov. 2005.

[45] M. Delcroix and R. Naeije, “Optimising the management of pulmonary arterial hypertension patients: emergency treatments.,” *Eur Respir Rev*, vol. 19, no. 117, pp. 204–11, Sep. 2010, doi: 10.1183/09059180.00004910.

[46] A. R. Tonelli *et al.*, “Causes and circumstances of death in pulmonary arterial hypertension.,” *Am J Respir Crit Care Med*, vol. 188, no. 3, pp. 365–9, Aug. 2013, doi: 10.1164/rccm.201209-1640OC.

[47] A. Rajdev, H. Garan, and A. Biviano, “Arrhythmias in pulmonary arterial hypertension.,” *Prog Cardiovasc Dis*, vol. 55, no. 2, pp. 180–6, 2012, doi: 10.1016/j.pcad.2012.06.002.

[48] N. Kanemoto and H. Sasamoto, “Arrhythmias in primary pulmonary hypertension.,” *Jpn Heart J*, vol. 20, no. 6, pp. 765–75, Nov. 1979, doi: 10.1536/ihj.20.765.

[49] R. W. Schrier and S. Bansal, “Pulmonary hypertension, right ventricular failure, and kidney: different from left ventricular failure?,” *Clin J Am Soc Nephrol*, vol. 3, no. 5, pp. 1232–7, Sep. 2008, doi: 10.2215/CJN.01960408.

[50] A. Algra, J. G. Tijssen, J. R. Roelandt, J. Pool, and J. Lubsen, “QTc prolongation measured by standard 12-lead electrocardiography is an independent risk factor for sudden death due to cardiac arrest.,” *Circulation*, vol. 83, no. 6, pp. 1888–94, Jun. 1991, doi: 10.1161/01.cir.83.6.1888.

[51] B. Strauss *et al.*, “Right predominant electrical remodeling in a pure model of pulmonary hypertension promotes reentrant arrhythmias.,” *Heart Rhythm*, vol. 19, no. 1, pp. 113–124, Jan. 2022, doi: 10.1016/j.hrthm.2021.09.021.

[52] J.-D. Fu and K. R. Laurita, “Repolarization Reserve and Action Potential Dynamics in Failing Myocytes.,” *Circ Arrhythm Electrophysiol*, vol. 11, no. 2, p. e006137, Feb. 2018, doi: 10.1161/CIRCEP.118.006137.

[53] Z. Husti, A. Varró, and I. Baczkó, “Arrhythmogenic Remodeling in the Failing Heart.,” *Cells*, vol. 10, no. 11, Nov. 2021, doi: 10.3390/cells10113203.

[54] S. Verheule and U. Schotten, “Electrophysiological Consequences of Cardiac Fibrosis.,” *Cells*, vol. 10, no. 11, Nov. 2021, doi: 10.3390/cells10113220.

[55] S. Andersen, J. E. Nielsen-Kudsk, A. Vonk Noordegraaf, and F. S. de Man, “Right Ventricular Fibrosis.,” *Circulation*, vol. 139, no. 2, pp. 269–285, Jan. 2019, doi: 10.1161/CIRCULATIONAHA.118.035326.

[56] S. Umar *et al.*, “Spontaneous ventricular fibrillation in right ventricular failure secondary to chronic pulmonary hypertension.,” *Circ Arrhythm Electrophysiol*, vol. 5, no. 1, pp. 181–90, Feb. 2012, doi: 10.1161/CIRCEP.111.967265.

[57] C. M. Suen, K. R. Chaudhary, Y. Deng, B. Jiang, and D. J. Stewart, “Fischer rats exhibit maladaptive structural and molecular right ventricular remodelling in severe pulmonary hypertension: a genetically prone model for right heart failure.,” *Cardiovasc Res*, vol. 115, no. 4, pp. 788–799, Mar. 2019, doi: 10.1093/cvr/cvy258.

[58] R. M. Bell, M. M. Mocanu, and D. M. Yellon, “Retrograde heart perfusion: the Langendorff technique of isolated heart perfusion.,” *J Mol Cell Cardiol*, vol. 50, no. 6, pp. 940–50, Jun. 2011, doi: 10.1016/j.yjmcc.2011.02.018.

[59] P. Lee, C. Bollensdorff, T. A. Quinn, J. P. Wuskell, L. M. Loew, and P. Kohl, “Single-sensor system for spatially resolved, continuous, and multiparametric optical mapping of cardiac tissue.,” *Heart Rhythm*, vol. 8, no. 9, pp. 1482–91, Sep. 2011, doi: 10.1016/j.hrthm.2011.03.061.

[60] E. M. Annoni *et al.*, “Intermittent electrical stimulation of the right cervical vagus nerve in salt-sensitive hypertensive rats: effects on blood pressure, arrhythmias, and ventricular electrophysiology.,” *Physiol Rep*, vol. 3, no. 8, Aug. 2015, doi: 10.14814/phy2.12476.

[61] N. Luqman, R. J. Sung, C.-L. Wang, and C.-T. Kuo, “Myocardial ischemia and ventricular fibrillation: pathophysiology and clinical implications.,” *Int J Cardiol*, vol. 119, no. 3, pp. 283–90, Jul. 2007, doi: 10.1016/j.ijcard.2006.09.016.

[62] C. Bonometti *et al.*, “Interaction between strong electrical stimulation and reentrant wavefronts in canine ventricular fibrillation.,” *Circ Res*, vol. 77, no. 2, pp. 407–16, Aug. 1995, doi: 10.1161/01.res.77.2.407.

[63] L. C. Pan, D. W. Wilson, and H. J. Segall, “Strain differences in the response of Fischer 344 and Sprague-Dawley rats to monocrotaline induced pulmonary vascular disease.,” *Toxicology*, vol. 79, no. 1, pp. 21–35, Mar. 1993, doi: 10.1016/0300-483x(93)90203-5.

[64] C. V Remillard *et al.*, “Function of Kv1.5 channels and genetic variations of KCNA5 in patients with idiopathic pulmonary arterial hypertension.,” *Am J Physiol Cell Physiol*, vol. 292, no. 5, pp. C1837-53, May 2007, doi: 10.1152/ajpcell.00405.2006.

[65] G. Pousada, A. Baloira, C. Vilariño, J. M. Cifrian, and D. Valverde, “Novel mutations in BMPR2, ACVRL1 and KCNA5 genes and hemodynamic parameters in patients with pulmonary arterial hypertension.,” *PLoS One*, vol. 9, no. 6, p. e100261, 2014, doi: 10.1371/journal.pone.0100261.

[66] O. Schmidlin, S. Bharati, M. Lev, and J. B. Schwartz, “Effects of physiological aging on cardiac electrophysiology in perfused Fischer 344 rat hearts.,” *Am J Physiol*, vol. 262, no. 1 Pt 2, pp. H97-105, Jan. 1992, doi: 10.1152/ajpheart.1992.262.1.H97.

[67] J. J. Rodriguez-Arias and A. García-Álvarez, “Sex Differences in Pulmonary Hypertension.,” *Frontiers in aging*, vol. 2, p. 727558, 2021, doi: 10.3389/fragi.2021.727558.